MULTIPLE DOCKING OF FLUORESCENT DYES TO FIBRILLAR INSULIN†

Uliana Tarabara*, Olga Zhytniakivska, Kateryna Vus,
Valeriya Trusova, Galyna Gorbenko

Department of Medical Physics and Biomedical Nanotechnologies, V.N. Karazin Kharkiv National University
4 Svobody Sq., Kharkiv, 61022, Ukraine
* *Corresponding Author: uliana.tarabara@karazin.ua*
Received August 1, 2022; revised August 18, 2022; accepted August 28, 2022

The co-localization of the donor and acceptor fluorophores capable of transferring the energy by the Förster mechanism, on the molecular scaffold of amyloid fibrils offers new opportunities not only for refinement of the amyloid detection and structural analysis, but also for designing photonic nanodevices on their basis. The assembly of these systems involves the non-covalent dye-protein interactions which can hardly be characterized in terms of a precise dye location within the fibril structure that is required for fabricating the FRET-based light harvesting systems or photonic nanowires. In view of this, the dye-fibril binding process deserves a detailed *in silico* study. In the previous molecular docking studies of the FRET donors and acceptors interacting with the insulin model fibrils we considered only one ligand during the simulation procedure. However, the real situation is much more complicated, when the multiple ligands can compete for the same binding site, a direct complexation between the dyes on the fibril scaffold can take place, the spatial distribution of the bound fluorophores can be unfavorable for the energy transfer, etc. In addition, the mutual orientation of the donor and acceptor molecules essentially contribute to the efficiency of the Förster resonance energy transfer (FRET) in the investigated systems. The present study was undertaken to gain molecular docking insight into the binding of the donor (Thioflavin T) and acceptor (Congo Red or a phosphonium dye TDV) fluorophores to the insulin amyloid fibrils using the multiple docking approach. The employed PatcDock and SwissDock webserves provided evidence for the preferable association of all dyes with the fibril grooves. The protein-ligand interaction profiler (PLIP) was employed for analyzing the (InsF + ThT +CR) and (InsF + ThT + TDV) systems. The revealed binding modes and the types of the dye-fibril interactions may be of importance for a more detailed analysis of the FRET process in amyloid systems and may serve as a background for further *in silico* studies of the cascade FRET on the amyloid fibril scaffold.

Keywords: fibrillar insulin, Thioflavin T, Congo Red, phosphonium dye, molecular docking study
PACS: 87.14.C++c, 87.16.Dg

Amyloid fibrils, a special class of the β-structured protein aggregates, are now receiving considerable attention in view of their link with numerous human disorders [1] and a promising potential as a novel type of nanomaterials [2]. A peculiar architecture of amyloid assemblies in which the solvent-exposed grooves lined with amino acid side chains extend along the fibril axis, accounts for specific binding of amyloid-sensitive dyes, among which the most widely used are the benzothiazole dye Thioflavin T (ThT) and the azo dye Congo red (CR) [3-5]. In our previous study we demonstrated that ThT and CR can be employed jointly as a donor-acceptor pair in the fluorescence amyloid assay based on the Förster resonance energy transfer (FRET) [6]. Later on, we found that amyloid fibrils can serve as a molecular scaffold not only for one-step energy transfer, but also for multi-step FRET (msFRET) in the three- and four- chromophore systems [7-10]. In the examined FRET chains ThT was recruited as an input donor, squaraine dyes SQ1/SQ2/SQ3 as terminal acceptors, while dimethylaminochalcone [8], phosphonium [7, 10], benzanthrone dyes [9] and squaraine (SQ4) dyes play the role of relay fluorophores. These studies open the way not only for improvement of the amyloid detection assays, but also for the use of amyloid assemblies in nanophotonics. The revealed significant enhancement of FRET in the amyloid protein fold was interpreted in terms of the increased quantum yields and greater donor-acceptor spectral overlap in the fibril-bound state, particular spatial and orientational arrangement of the fluorophores constituting the energy transfer chain. In view of a high amyloid sensitivity of the FRET process, it seems reasonable to take a deeper look on the determinants of fibril-fluorophore interactions using the *in silico* tools. Among these, one of the most widespread is the molecular docking modulation technique capable of predicting the best way of the ligand-receptor interactions and affinity of small molecules to the target macromolecule [11]. During the simulation procedure the orientation and conformation of the ligand are changed to reach the global minimum of the ligand-macromolecule binding energy [12]. The molecular docking can be implemented by two ways: i) geometric search for the receptor surface regions complementary to ligand) [13], ii) docking simulation through evaluating the minimum in energy landscape by considering each binding mode) [14, 15]. A more sophisticated docking technique, multiple ligand simultaneous docking (MLSD), allows to perform the docking of several ligands to the same target, that is more realistic since water molecules and a variety of cofactors, substrates, ions can bind to biomacromolecules along with the main ligand [16, 17]. The optimized MLSD algorithm has been developed [16] that provides a sensitivity of ligands to the presence of each other. Since the two or more dyes are involved in the energy transfer, it is sensible to analyze the binding behavior of the donor and acceptor fluorophores using the multiple docking approach. In view of this, the aim of the present study was to

evaluate the possibility of simultaneous docking of the classic amyloid markers (ThT and CR) and one donor-acceptor pair from the previously examined msFRET chains (ThT – TDV) to the insulin amyloid fibrils.
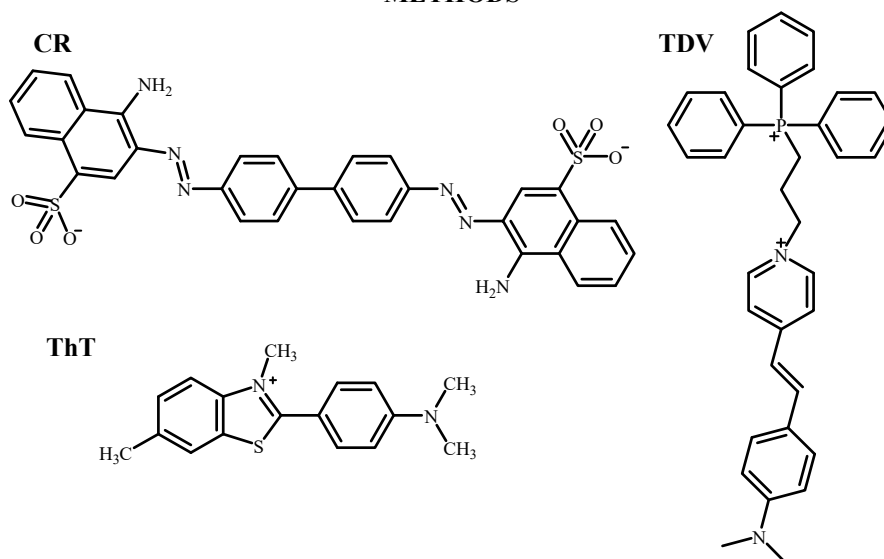
METHODS

Figure 1. Structural formulas of the examined dyes

The structures of three dyes under study (Fig. 1) were built in MarvinSketch (version 18.10.0) [18] and optimized in Avogadro (version 1.1.0) [19]. The counterions were not added to the dye structures in order to save the molecular charges. The model of the human insulin fibril (InsF) was obtained from http://people.mbi.ucla.edu/sawaya/jmol/fibrilmodels/. The input structure of the ThT complexes with fibrillar insulin for the next docking run (Fig. 2) was performed using the SwissDock server [20]. The free energy of the ThT-InsF binding (ΔG) was estimated to be -8.36 kcal/mol. To perform the docking of CR or TDV to the complex (InsF+ThT) we tried to use the two different webservers: PatchDock and SwissDock. The molecular docking algorithm underlying the PatchDock server target on the finding the maximal surface shape complementarity along with the minimal amounts of steric clashes [21]. The EADock DSS algorithm behind the SwissDock server computes and clustered the most favorable binding modes using the rigid docking procedure [20]. In order to identify the amino acid residues constituting the binding sites and to analyze the types of the dye-protein contacts, the protein-ligand interaction profiler (PLIP, https://plip-tool.biotec.tu-dresden.de/plip-web/plip/index) was employed. The selected docking poses were visualized with the UCSF Chimera software (version 1.14) [22].
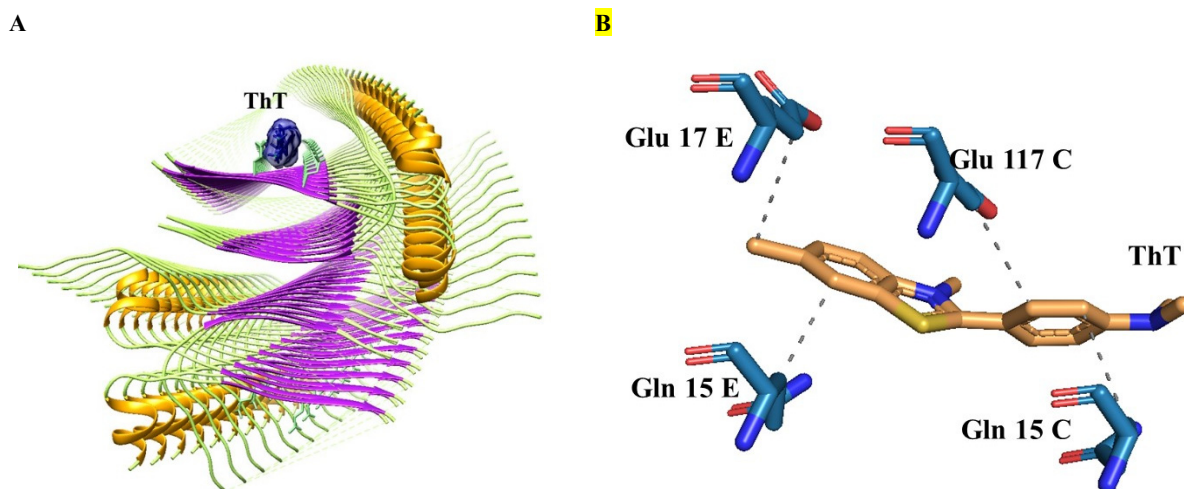
Figure 2. The (InsF + ThT) complex that was selected as input structure for the next docking run, visualized by the UCSF Chimera software (A) and analyzed in PLIP (B). The β-sheets and α-helixes are colored in violet and goldenrod, respectively, while ThT and the residues Gln15, Glu17 are marked by navy blue and light green, respectively (A). The gray dashed lines on the panel B represent the hydrophobic interactions between the dye molecule and the insulin residues.

RESULTS AND DISCUSSION

The PLIP analysis of the ThT complex with the groove Gln 15 – Glu 17 of the insulin fibrils revealed a predominant role of hydrophobic interactions between the dye and the residues (Gln 15 C, Gln 15 E, Glu 17E, Glu 117 C) (Fig. 2 B), that is in accord with the experimental studies of the ThT location within fibril structure [23, 24]. All the PatchDock solutions provided evidence for the CR binding in the cross-strand ladder formed by B 17 leucine residues located on the dry steric zipper fibril interface (Fig. 3 A). The obtained results are similar to those previously reported for the complexes of cyanines [25, 26], DMC and ThT [8, 26] with the fibrillar insulin. The global energy for the most energetically favorable model was -132.95 kcal/mol, revealing both a very high stability of this complex *in silico* and a high probability of such mode of the dye-fibril association *in vitro*. The hydrophobic interactions between CR and the nonpolar residues (Ile 102 of S, U, W chains and Leu 306 of U, W, Y chains) of the fibrillar insulin, along with the hydrogen bonds between sulfonate and amino groups of the CR and both nonpolar (Val 218 X) and polar (Cys 219 T, Cys 307 W) residues were also uncovered by the PLIP analysis (Fig. 3 B).
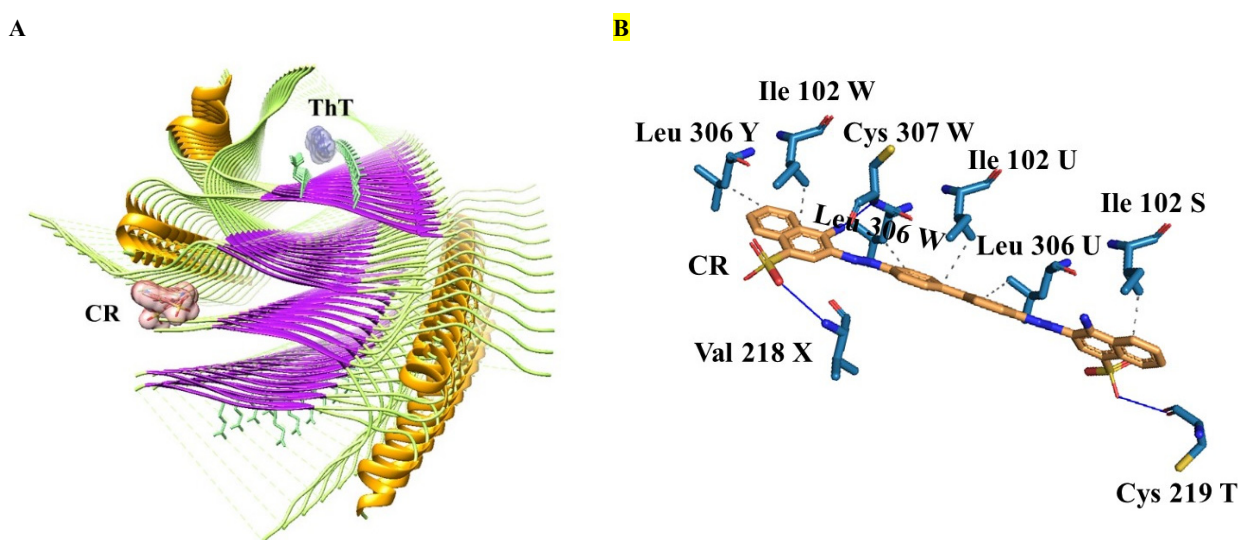

Figure 3. The energetically most favorable CR associate with the complex (InsF + ThT), obtained using the PatchDock webserver (A) and analyzed in PLIP (B). The CR and ThT are marked by red and navy blue, respectively. The gray dashed lines on the panel B represent the hydrophobic interactions between the dye molecule and the insulin residues, while the blue solid line displays the hydrogen bonds.

In contrast to the PatchDock results, the most CR docking poses revealed by the SwissDock are located near the groove Gln 15 – Glu 17 on the wet fibrillar surface and close to the residue Gln 204 belonging to the native-like N-terminus of the insulin B chain. One binging mode of this dye was in Q15 – E17 groove demonstrating the disposition of the CR along the long fibril axis, parallel to the selected ThT binding pose (Fig. 4 A, red). This complex with $\Delta G = -8.59$ kcal/mol is stabilized mainly by the hydrophobic contacts with the groove residues of the D, F, H chains and hydrogen bonds between functional groups of the dye and Leu 16, Gln 204, in addition to Gln 15 and Glu 17 (Fig. 4 B). The binding mode with the minimal free energy of binding ($\Delta G = -9.36$ kcal/mol) involves a partial intercalation of Congo Red in the groove by the naphthalene ring (Fig. 4 A, yellow). Therefore, the possibility of almost perpendicular dye orientation relative to ThT cannot be excluded. A significant amount of hydrogen bonds (Gln 15 L, Glu 117 J, Phe 201 H, Gln 204 J) were found to participate in the formation of this complex (Fig. 4 C). The distinguishable and non-specific binding site located at the native-like N-terminus of the insulin B chain is represented in Figs. 4 A (green CR structure) and 4 D. According to this model, Congo Red molecules are buried between Gln 304 and Leu 306 interacting with them and the neighboring His 305 by both hydrophobic and electrostatic (hydrogen bonds and salt bridges) forces. This binding mode can be explained by the rigid structure of receptor during the docking procedure, while the great flexibility of these non-extended N-terminal tails of the chain B (in comparison to the native insulin) can be expected *in vitro*, that with high probability may lead to the disruption of the cavity Gln 304 - Leu 306 [27].

It should be noted that the ThT molecule seems to be removed in the SwissDock output files, indicating that this server is not suitable for the multiple ligand simultaneous docking. Therefore, a more appropriate technique like AutoDock 4.0 [28, 16] is planned to be used in the further studies for a more precise analysis of the simultaneous docking results and, ideally, description of the ligand-ligand interactions. Nevertheless, the differences in the algorithms, technical realization, numerous docking runs provide a good opportunity for considering the dye-protein interactions more comprehensively.
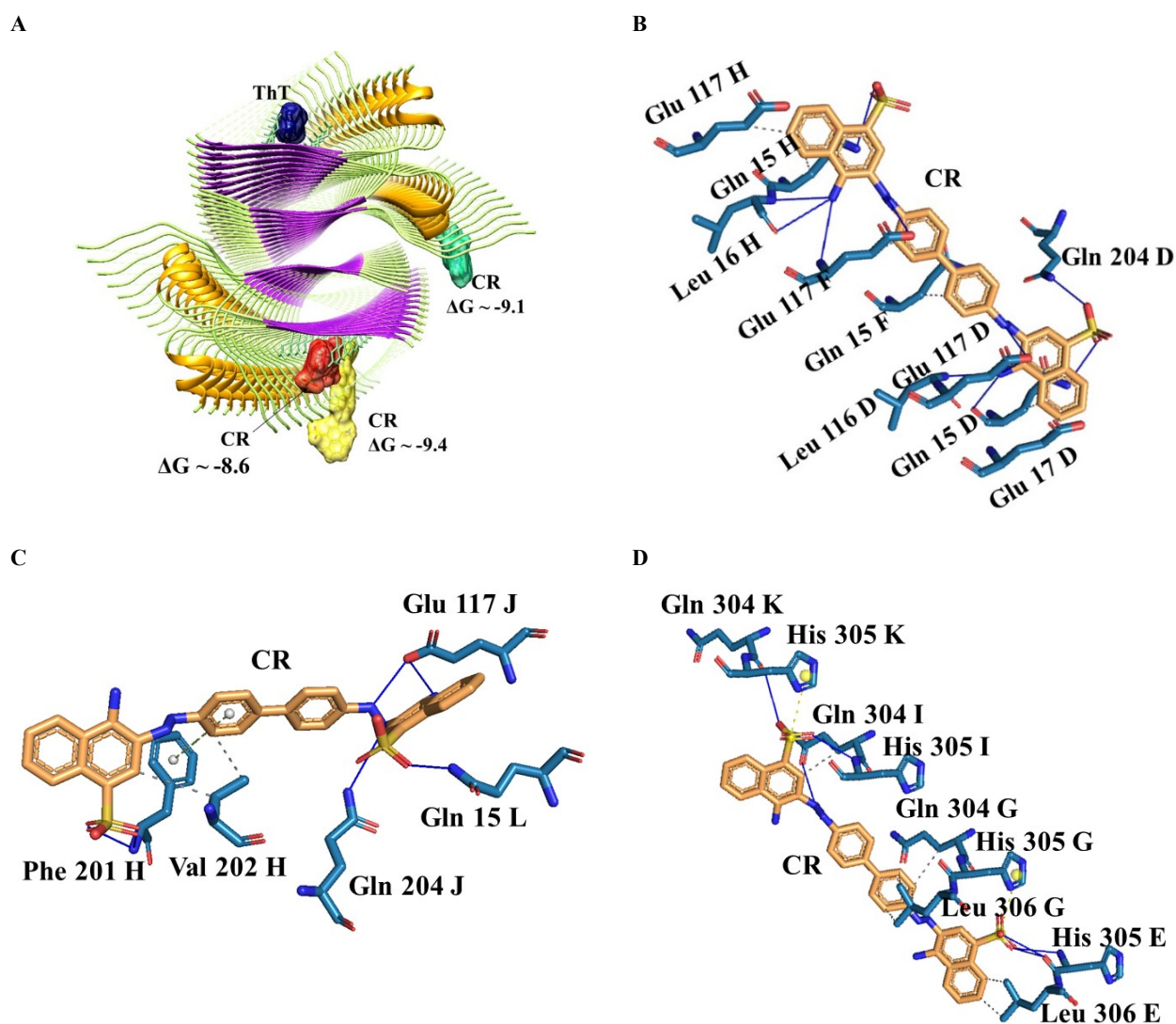
Figure 4. Representative modes of interactions between CR and the complex (InsF + ThT), obtained using the SwissDock server (A) and analyzed in PLIP (B -D). ThT is marked by navy blue (A). The docking energies for selected complexes are -8.59 kcal/mol (CR is marked by red on the panel A, PLIP results are depicted on the panel B), -9.36 kcal/mol (yellow, C), -9.07 kcal/mol (green, D). The gray dashed lines on the panels B, C and D represent the hydrophobic interactions between the dye molecule and the insulin residues, while the green dashed line, yellow dashed line and blue solid line display the π-stacking contacts, salt bridges and hydrogen bonds, respectively.

At the next step of study, the interaction of the phosphonium dye TDV with the complex (InsF + ThT) was explored using the above approaches. According to the PatchDock, this dye can be located in the grooves Gln 15 – Glu 17 (Fig. 5 A red) and Tyr19 – Asn21 (Fig. 5 A green), as well as can reside in the area between the native-like N-terminal tails of the chain B and outer β-sheet formed by the LYQLENY segment from the A chain. The binding mode with higher value of the global energy (-37.19 kcal/mol) is depicted in Figure 5 A (violet). This complex is stabilized by a large number of hydrophobic contacts between TDV and nonpolar (Ile 2 D, Leu 13 D, Leu 13 F, Val 202 D, Leu 206 D), polar (Gln 204 B, Gln 204 B, Gln 204 D), aromatic (Phe 201 B, Phe 201 D) and positively charged (His 205 B) residues (Fig. 5 D). The π-stacking contact (His 205 B) was also observed, while the other selected docking poses (Fig. 5 B, C) are stabilized mainly by hydrophobic interactions with the groove residues.

Most binding modes obtained by the SwissDock suggest that TDV is localized on the wet surface of fibril structure (data not shown). The more energetically favorable complexes (ΔG ≤ -8.4 kcal/mol) revealed the TDV orientation in which one benzene ring of phosphonium group is directed to the groove Q15 – E17, while the rest of the dye molecule is intercalated between N-terminal parts of the chains constituting the fibril periphery. The PLIP analysis indicates that the complex (InsF + TDV) is stabilized by hydrophobic contacts, hydrogen bonds and π-stacking interactions preferably with the residues of the non-extended fibril part such as Gly 1, Ile 2, Val 3, Gln 5, Phe 201, Val 202, Gln 204, His 205) than Gln 15 and Glu 17.
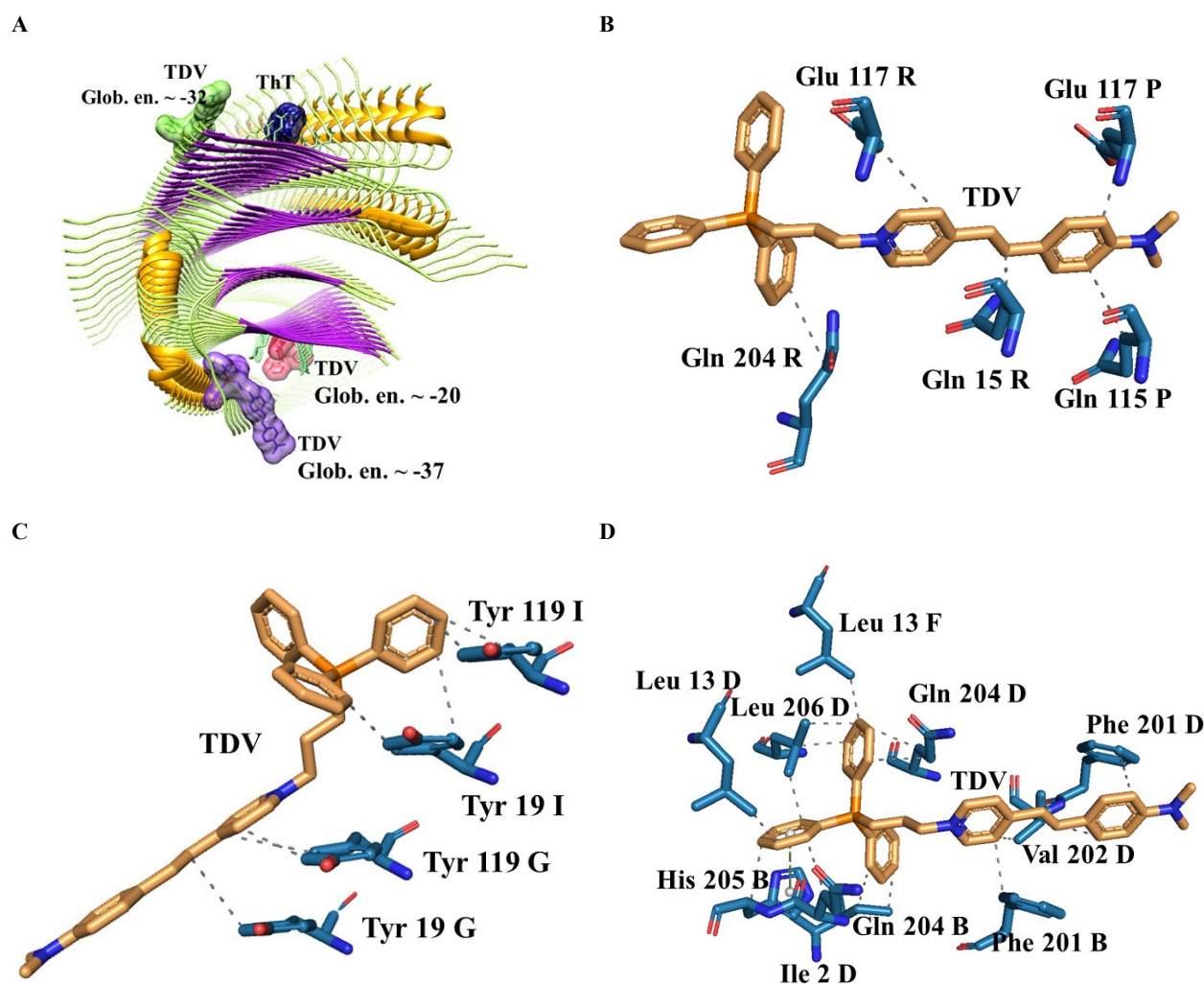
Figure 5. Representative modes of interactions between TDV and the complex (InsF + ThT), obtained using the PatchDock webserver (A) and analyzed in PLIP (B -D). ThT is marked by navy blue (A). The global energies for selected complexes are -20.4 kcal/mol (TDV is marked by red on the panel A, PLIP results are depicted on the panel B), -31.99 kcal/mol (green, C), -37.19 kcal/mol (violet, D). The gray dashed lines on the panels B, C and D represent the hydrophobic interactions between the dye molecule and the insulin residues, while yellow dashed line displays the salt bridges.

CONCLUSIONS

To summarize, the present study was focused on the investigation of the interactions between the FRET acceptor dyes CR or TDV and the insulin amyloid fibrils hosting the donor dye ThT using the two webservers: PatchDock and SwissDock. The binding sites of the (InsF+ThT) complex for the examined dyes, as well as the types of the dye-protein interactions were identified. Based on the acquired results, the following assumptions can be made: i) regardless of the cationic nature of ThT and TDV molecules, and the negative charge of CR, the dye-protein complexes are stabilized by hydrophobic, rather than electrostatic interactions; ii) the dye location along the surface side-chain grooves Q15 - E17 (CR, TDV), Y19 – N21 (TDV) is in line with the previously proposed binding mode and provides almost parallel orientation of the fluorophore transition dipoles; iii) the existence the binding site such as native-like N-terminus and cross-strand ladder on the dry steric zipper interface that is characterized by the lower docking energy than the fibril grooves does not rule out the other orientations of the donor and acceptor transition dipoles, as well as point to the existence of different binding sites for ThT and the FRET acceptors such as CR and TDV, reducing the probability of the competition between the dyes. Overall, our findings may be useful for a deeper understanding of the factors controlling the binding and orientational behavior of the donor and acceptor fluorophores involved in the energy transfer on the amyloid fibril scaffold.

ORCID IDs
Ⓘ**Uliana Tarabara**, https://orcid.org/0000-0002-7677-0779; Ⓘ**Olga Zhytniakivska**, https://orcid.org/0000-0002-2068-5823
Ⓘ**Kateryna Vus**, https://orcid.org/0000-0003-4738-4016; Ⓘ**Valeriya Trusova**, https://orcid.org/0000-0002-7087-071X
Ⓘ**Galyna Gorbenko**, https://orcid.org/0000-0002-0954-5053

REFERENCES

[1]   F. Chiti, and C.M. Dobson, Annu. Rev. Biochem. **75**, 333 (2006), https://doi.org/10.1146/annurev.biochem.75.101304.123901
[2]   T.P. Knowles, and R. Mezzenga, Adv. Mater. **28**, 6546 (2016), https://doi.org/10.1002/adma.201505961
[3]   W.E. Klunk, J. Histochem. Cytochem. **37**, 1273 (1989), https://doi.org/10.1177/37.8.2666510
[4]   M.R.H. Krebs, E.H.C. Bromley, and A.M. Donald, J. Struct. Biol. **149**, 30–37 (2005) https://doi.org/10.1016/j.jsb.2004.08.002
[5]   M. Groenning, J. Chem. Biol. **3**, 1–18 (2010), https://doi.org/10.1007/s12154-009-0027-5
[6]   M. Girych, G. Gorbenko, I. Maliyov, V. Trusova, C. Mizuguchi, H. Saito, and P. Kinnunen, Methods Appl. Fluoresc. **4**, 034010 (2016). https://doi.org/10.1088/2050-6120/4/3/034010
[7]   G. Gorbenko, V. Trusova, T. Deligeorgiev, N. Gadjev, C. Mizuguchi, and H. Saito, J. Mol. Liq. **294**, 111675 (2019), https://doi.org/10.1016/j.molliq.2019.111675
[8]   U. Tarabara, M. Shchuka, K. Vus, O. Zhytniakivska, V. Trusova, G. Gorbenko, N. Gadjev, and T. Deligeorgiev, East Eur. J. Phys. **4**, 58 (2019), https://doi.org/10.26565/2312-4334-2019-4-06
[9]   U. Tarabara, E. Kirilova, G. Kirilov, K. Vus, O. Zhytniakivska, V. Trusova, and G. Gorbenko, J. Mol. Liq. **324**, 115102 (2021), https://doi.org/10.1016/j.molliq.2020.115102
[10]   G. Gorbenko, O. Zhytniakivska, K. Vus, U. Tarabara, and V. Trusova, Phys. Chem. Chem. Phys. **23**, 14746 (2021), https://doi.org/10.1039/D1CP01359A
[11]   T. Lengauer, and M. Rarey, Curr. Opin. Struct. Biol. **6**, 402 (1996), https://doi.org/10.1016/S0959-440X(96)80061-3
[12]   P.F. Leonhart, E. Spieler, R. Ligabue-Braun, and M. Dorn, Soft Comput. **23**, 4155 (2019), https://doi.org/10.1007/s00500-018-3065-5
[13]   S.F. Sousa, P.A. Fernandes, and M.J. Ramos, PROTEINS: Structure, Function, and Bioinformatics, **65**, 15 (2006), https://doi.org/10.1002/prot.21082
[14]   R. Huey, G.M. Morris, A.J. Olson, and D.S. Goodsell, J. Computational Chemistry, 28, 1145 (2007), https://doi.org/10.1002/jcc.20634
[15]   H. Li, PhD Thesis, (2012), https://etd.ohiolink.edu/
[16]   H. Li, and C. Li, J. Computational Chemistry, **31**, 2014 (2010), https://doi.org/10.1002/jcc.21486
[17]   S. Raghavendra, S.J. Rao Aditya, Vadlapudi Kumar, and C.K. Ramesh, Computational Biology and Chemistry. **59**, Part A, 81 (2015), https://doi.org/10.1016/j.compbiolchem.2015.09.008
[18]   P. Csizmadia, in: *Proceedings of ECSOC-3, The Third International Electronic Conference on Synthetic Organic Chemistry*, (MDPI, Basel, Switzerland, 1999), pp. 367-369. https://doi.org/10.3390/ecsoc-3-01775
[19]   M.D. Hanwell, D.E. Curtis, D.C. Lonie, T. Vandermeersch, E. Zurek, and G.R. Hutchison, J. Cheminform. **4**, 17 (2012), https://doi.org/10.1186/1758-2946-4-17
[20]   A. Grosdidier, V. Zoete, and O. Michielin, Nucleic Acids Res. **39**, W270 (2011), https://doi.org/10.1093/nar/gkr366
[21]   D. Schneidman-Duhovny, Y. Inbar, R. Nussinov, and H.J. Wolfson, Nucl. Acids. Res. **33**, W363 (2005), https://doi.org/10.1093/nar/gki481
[22]   E.F. Pettersen, T.D. Goddard, C.C. Huang, G.S. Couch, D.M. Greenblatt, E.C. Meng, and T.E. Ferrin, J. Comput. Chem. **25**, 1605 (2004), https://doi.org/10.1002/jcc.20084
[23]   M. Biancalana, and S. Koide, Biochim. Biophys. Acta, **1804**, 1405 (2010), https://doi.org/10.1016/j.bbapap.2010.04.001
[24]   C. Wu, M. Biancalana, S. Koide, and J.E. Shea, J. Mol. Biol. **394**, 627 (2009), https://doi.org/10.1016/j.jmb.2009.09.056
[25]   O. Zhytniakivska, A. Kurutos, U. Tarabara, K. Vus, V. Trusova, G. Gorbenko, N. Gadjev, and T. Deligeorgiev, J. Mol. Liq. **311**, 113287 (2020) https://doi.org/10.1016/j.molliq.2020.113287
[26]   K. Vus, M. Girych, V. Trusova, G. Gorbenko, A. Kurutos, A. Vasilev, N. Gadjev, and T. Deligeorgiev, J. Mol. Liq. **276**, 541 (2019), https://doi.org/10.1016/j.molliq.2018.11.149
[27]   M.I. Ivanova, S.A. Sievers, M.R. Sawaya, J.S. Wall, and D. Eisenberg, PNAS. **106**, 18990–18995 (2009), https://doi.org/10.1073/pnas.0910080106
[28]   S. Forli, R. Huey, M.E. Pique, M. Sanner, D.S. Goodsell, and A.J. Olson, Nat. Protoc. **11**, 905 (2016), https://doi.org/10.1038/nprot.2016.051

МУЛЬТИМОЛЕКУЛЯРНИЙ ДОКІНГ ФЛУОРЕСЦЕНТНИХ БАРВНИКІВ З ФІБРИЛЯРНИМ ІНСУЛІНОМ
У. Тарабара, О. Житняківська, К. Вус, В. Трусова, Г. Горбенко

Кафедра медичної фізики та біомедичних нанотехнологій, Харківський національний університет імені В.Н. Каразіна
м. Свободи 4, Харків, 61022, Україна

Колокалізація донорів та акцепторів флуорофорів, здатних переносити енергію за механізмом Фьорстера, на молекулярній матриці амілоїдних фібрил, відкриває нові можливості не тільки для вдосконалення детекції амілоїдних фібрил та структурного аналізу, але і для розробки фотонних наноприладів на їх основі. Збірка цих систем передбачає нековалентні взаємодії барвник-білок, які складно охарактеризувати з точки зору точного розташування барвника в структурі фібрили, необхідного для виготовлення світлозбиральних систем чи фотонних нанодротів на основі Фьорстерівського резонансного переносу енергії (ФРПЕ). З огляду на це, процес зв'язування барвників з фібрилами доцільно детально проаналізувати *in silico*. У попередніх дослідженнях донорів та акцепторів ФРПЕ, що взаємодіяли з модельними фібрилами інсуліну, методом молекулярного докінгу, під час процедури моделювання ми розглядали лише один ліганд. Однак реальна ситуація набагато складніша, оскільки кілька лігандів можуть конкурувати за один і той же сайт зв'язування, може відбуватись пряме комплексоутворення між барвниками на матриці фібрил, просторовий розподіл зв'язаних флуорофорів може бути несприятливим для передачі енергії тощо. Крім того, взаємна орієнтація молекул донора та акцептора вносить суттєвий вклад в ефективність Фьорстерівського резонансного переносу енергії у досліджуваних системах. Дана робота була проведена, щоб отримати уявлення про зв'язування донорних (Тіофлавін Т) і акцепторних (Конго Червоний або фосфонієвий барвник TDV) флуорофорів з амілоїдними фібрилами інсуліну за допомогою підходу мультимолекулярного докінгу. Використані веб-сервери PatcDock і SwissDock надали докази переважної асоціації всіх барвників із жолобками фібрил. Для аналізу систем (InsF + ThT +CR) і (InsF + ThT + TDV) використовувався protein-ligand interaction profiler (PLIP). Виявлені сайти зв'язування та типи взаємодій між барвниками та фібрилою можуть бути важливими для більш детального аналізу процесу ФРПЕ в амілоїдних системах і можуть слугувати основою для подальших досліджень *in silico* каскаду ФРПЕ на матриці амілоїдних фібрил.
Ключові слова: фібрилярний інсулін, Тіофлавін Т, Конго Червоний, фосфонієвий барвник, молекулярний докінг

CALCULATION OF THE ABSORBED DOSE BY A BOROSILICATE GLASS MATRIX AND ITS SIMULATED IRRADIATION†

Volodymyr Morgunov[a]*, Serhii Sayenko[b], Volodymyr Shkuropatenko[b], Yevhenii Svitlychnyi[b], Olena Bereznyak[b], Serhii Lytovchenko[a], Volodymyr Chyshkala[a]

[a]V.N. Karazin Kharkiv National University, 4 Svobody Sq., Kharkiv, 61022, Ukraine
[b]NSC "Kharkiv Institute of Physics and Technology", 1 Akademicheskaya St., Kharkiv, 61108, Ukraine
*Corresponding Author: v.morgunov@karazin.ua

The state of liquid radioactive wastes (LRW) management at Ukrainian Nuclear Power Plants (NPPs) is characterized by the lack of a completed technological cycle from processing to obtaining the final product suitable for further long-term storage or disposal. As a result, the storage tanks for bottoms residue (BR) are 65-75% full (Zaporizhzhia and South-Ukrainian NPPs), and the resource for placing molten salt at Zaporizhzhya NPP (92.7%) is close to exhaustion. Therefore, the development of technologies and materials for NPP LRW solidification is an urgent need and aims to ensure the processing of LRW to a solid state that will meet the acceptance criteria for disposal in centralized storage facilities. One of the effective methods of LRW solidification is their vitrification. The main advantage of vitrification is that during the vitrification process the volume of waste is reduced by several times and this saves expensive storage space. The purpose of this work is to calculate the absorbed dose that borosilicate glass matrices with included bottoms residue will accumulate over 300 years of storage, and to study the effect of simulated X-ray irradiation on their physical and mechanical properties.

Keywords: liquid radioactive wastes, bottoms residue, borosilicate glass matrices, absorbed dose, numerical simulation.
PACS: 28.41.Kw; 28.41.Te; 02.70.Uu

INITIAL CONDITIONS

In Ukraine today, more than 19 000 m^3 of liquid radioactive waste has been accumulated at nuclear power plants. Due to the lack of technical solutions that ensure the receipt of the final product acceptable for disposal for disposal, with the current dynamics of LRW receipts, the resource of LRW storage tanks is close to exhaustion [1]. It is believed that the most optimal method of LRW solidification is their vitrification followed by storage in surface storage facilities [2, 3].

The following data were taken for calculations through the article: specific activities of isotopes ^{137}Cs, ^{134}Cs and ^{60}Co in BR are given in Table 1. The half-lives and decay constants of these isotopes are given in Table 2. The chemical composition of borosilicate glass is given in Table 3

Table 1. Initial data

Parameters	Value
Specific activity of isotopes:	
^{137}Cs, 10^{-6} Ci/l	52
^{134}Cs, 10^{-6} Ci/l	28
^{60}Co, 10^{-6} Ci/l	6,1
Period of simulation, years	300

Table 2. The half-lives and decay constants ^{137}Cs, ^{134}Cs and ^{60}Co

Isotope	Half-lives, days	Decay constant, λ
^{137}Cs	11000±90	0.0000630
^{134}Cs	754±0.7	0.0009197
^{60}Co	1925.3±0.4	0.0003601

Table 3. The chemical composition of borosilicate glass

Name of oxide	Content, mass. %	Density, kg/m^3
B_2O_2	11.49	2460
Na_2O	27.64	2300
MgO	0.43	3600
Al_2O_3	0.98	3950
SiO_2	45.67	2648
P_2O_5	0.072	2390
SO_2	0.45	2619

Name of oxide	Content, mass. %	Density, kg/m³
Cl_2O_3	0.21	1600
K_2O	3.55	2300
CaO	0.94	3340
TiO_2	0.037	4230
Fe_2O_3	0.36	5240
Cu_2O	0.036	6000
Cs_2O	0.58	4650
PbO	7.55	9640

DESCRIPTION OF THE SAMPLES PREPARATION AND THEIR IRRADIATION

Samples of the borosilicate glass matrix were obtained by preliminary melting of a mixture of a calcined solution – simulator of NPP LRW condensate with VVER-1000 reactors with the addition of glass-forming silicon oxide, in the form of sand, and 10 wt. % lead oxide (SK45-Pb10) or calcium fluoride (SK45-CF10), followed by melting and pouring glass into metal molds. At the same time, it was taken into account that since the content of Na and B in the bottom residues of LRW from nuclear power plants with VVER reactors is quite high, there is no need to add these elements to obtain borosilicate glass matrices [4]. According to the results of XRD and SEM studies, it was determined that the resulting glass matrices are X-ray amorphous, do not have crystalline inclusions, and are characterized by a dense and homogeneous structure.

Simulated X-ray irradiation of samples of the borosilicate glass matrix was carried out on a linear electron accelerator LU-10 (NSC KIPT) using bremsstrahlung radiation. The average energy of photons is 10.4 MeV. The dose rate is equal 1.09 kGy per hour.

Taking into account the fact that the activity of bottom residues of NPP LRW can differ markedly depending on the methods of LRW processing used at individual NPPs, and, moreover, the distribution of radionuclides in the matrix can be uneven, which can increase the dose of self-irradiation of individual glass blocks, simulation irradiation was carried out with an increased absorption dose – 10 kGy and 100 kGy.

DESCRIPTION OF THE NUMERICAL SIMULATION

For calculation of absorbed dose received by borosilicate glass matrices with included bottoms residue we used software toolkit GEANT4, a toolkit for the simulation of the passage of particles through matter. Its areas of application include high energy, nuclear and accelerator physics, as well as studies in medical and space science [5–7]. To use GEANT4 the following aspects should be defined:
– the geometry of the system;
– the materials and chemical elements involved;
– the fundamental particles of interest;
– the physical processes of interest;
– the generation of primary events;
– the response of sensitive detector components.

The geometry of the system

The geometry of the systems involves the dimensions of the objects and their location. For the calculation three types of setups were chosen:

Setup 1. The cube with dimensions 2 cm × 2 cm × 2 cm with radioactive sources as spheres with diameter 0.5 mm located inside the cube with following coordinates: 1st source (^{137}Cs) – {0; 2 mm; 2 mm}, 2nd source (^{60}Co) – {0; 0; 0}, 3d source (^{134}Cs) – {0; -2 mm; -2 mm}. The absorbed dose was calculated for whole cube.

Setup 2. The absorbed dose was calculated for the cube with the dimensions 10 cm × 10 cm × 10 cm located in the center of a cylinder (height – 812 mm, radius – 560 mm) which consist of a borosilicate glass (Fig. 1). Radiation sources are uniformly dispersed through the cylinder.

Setup 3. The dose map was calculated for cross-section of the same cylinder as item 2 (Fig. 2). Radiation sources are uniformly dispersed through the cylinder.
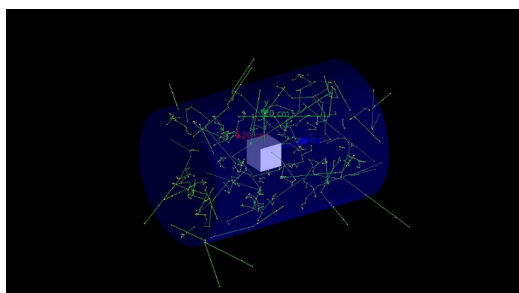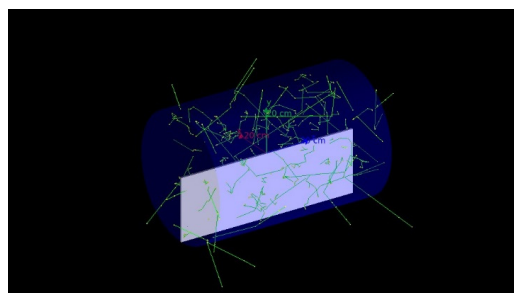

Figure 1. Setup No 2 (see text)

Figure 2. Setup No 3

The materials and chemical elements involved

The following materials are involved into the simulation:
– borosilicate glass matrix (chemical composition is given in Table 3);
– radioactive isotopes ^{137}Cs, ^{134}Cs, ^{60}Co.

The fundamental particles of interest

According to the physical laws during gamma irradiation following elementary particles take part:

– gamma rays;
– X rays;
– electrons;
– positrons;
– anti-neutrinos.

Anti-neutrinos are not included into simulation because these particles can pass through the matter without any collisions with the matter.

The physical processes of interest

Seven major categories of processes are provided by GEANT4:

1. electromagnetic;
2. hadronic;
3. decay;
4. photolepton-hadron;
5. optical;
6. parameterization;
7. transportation.

In the simulation, the 1st, 3^{d} and 7th processes were chosen.

The generation of primary events

Generation of initial gamma rays are generated from ^{137}Cs, ^{134}Cs and ^{60}Co isotropically according to specific activities given in Table 2. Built-in GEANT4 General Particle Source (GPS) class is used for this purpose. The decay of isotopes (see Table 2) is taken into the account in the simulation.

The response of sensitive detector components

To record and output data from simulations, a process called "scoring", must be implemented, specifying what should be measured and where.

In the simulation absorbed doses were calculated for the borosilicate glass itself: for Setup1 absorbed dose was calculated for whole cube; for Setup 2 absorbed dose was calculated for cube inside cylinder; for Setup 3 absorbed dose was calculated for half of cross-section. All values of absorbed dose are referenced to the water.

RESULTS OF NUMERICAL CALCULATION

Calculations were performed on personal computer equipped with AMD Ryzen™9 3900xt (24 threads, 12 cores) processor, 48 GB RAM.

Amount of simulated events was 10^7. For every half of year activities of isotopes recalculated according to the following radioactive decay law

$$I - I_0 e^{-\lambda t}$$

(1)

where, I_0 – initial activity, Ki; λ – decay constant; t – time elapsed since the initial moment of time, days. Absorbed dose calculated according to the following formula

$$D = \frac{k \cdot d \cdot \sum I \cdot V}{n_0}$$

(2)

where $k = 3.7 \cdot 10^7$ – number of decays per 1 second (corresponds to 1 Ci); d – calculated absorbed dose; ΣI – total activity of all radioactive sources at the time of calculation (taking into account radioactive decay), Ci/m^3; V – volume of the target being modeled, m^3; n_0 – the number of decays (10^7) that was modeled. The results of calculations for 300 years of long-term storage of nuclear waste are given on Fig. 3. The initial data are given in the Tables 1 and 2. The absorbed dose in cylinder (height - 0.8 and radius - 0.28 m) is equal to 627.9 Gy for 300 years.
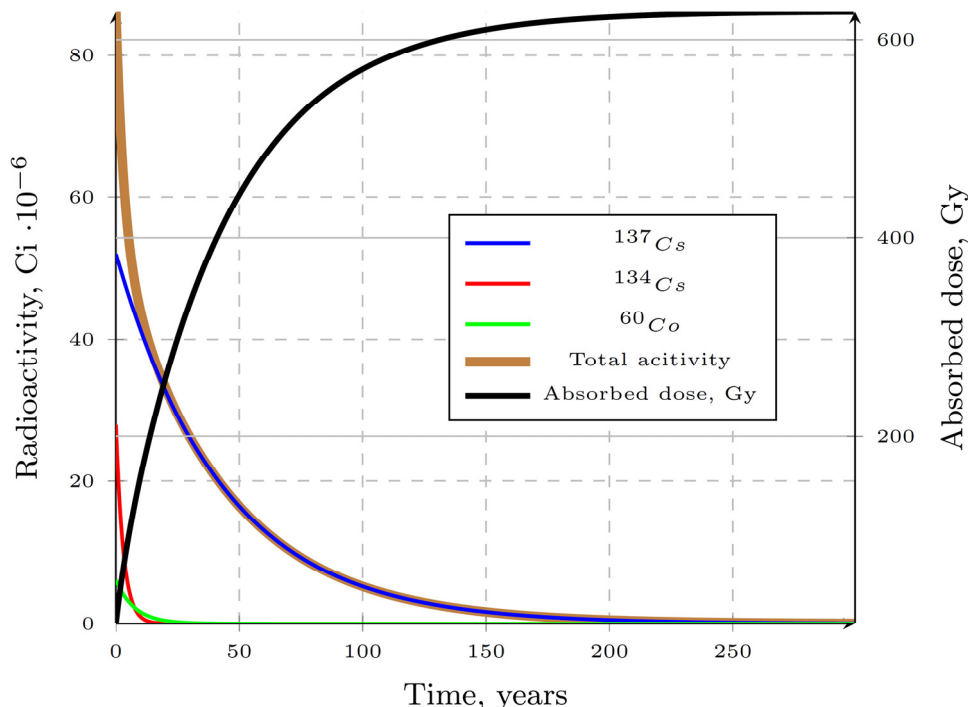

Figure 3. Radioactivities of ^{137}Cs, ^{134}Cs, ^{60}Co, total radioactivity, absorbed dose vs time

RESULTS OF THE SIMULATED IRRADIATION

Simulated irradiation of samples of the borosilicate glass matrix was carried out on a linear electron accelerator LU-10 (NSC KIPT) using bremsstrahlung X-ray radiation. The average energy of photons is 10.4 MeV. The rate of collection of the absorbed radiation dose is 1.09 kGy per hour.

After the simulated irradiation, the structure and phase composition of the SK45-Pb10 and SK45-CF10 glass matrix samples were studied. As can be seen from Fig. 4, the appearance of the samples of borosilicate glass matrices SK45-Pb10 and SK45-CF10 irradiated with X-ray did not differ from the samples before irradiation, except for color. Samples for irradiation have a green transparent colour, while after irradiation their colour has changed to opaque black. As is known, most types of glass lose their transparency under the influence of X ray irradiation. Exposure to this type of radiation leads to colouration of the glass throughout its entire thickness.
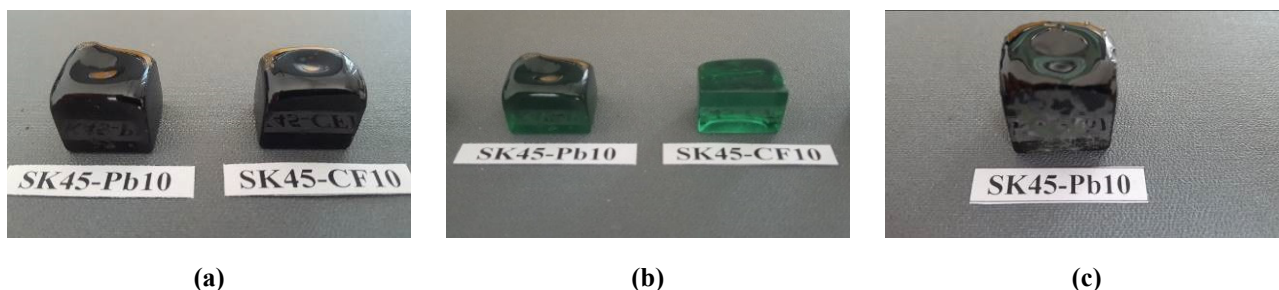

(a)   (b)   (c)

Figure 4. Samples of glass matrices SK45-Pb10 and SK45-CF10
a – before irradiation, b – after 10 kGy irradiation, c – after 100 kGy irradiation

There are no signs of destruction and the appearance of cracks and other defects on the samples after irradiation. Also, no changes were observed in the structure (Fig. 5a) and phase composition of the SK45-Pb10 glass matrix samples after irradiation to an absorbed dose of 100 kGy (Fig. 5b). The glass matrix material remains X-ray amorphous without the appearance of crystalline phases.

Small differences were found in the IR spectra of glass matrix samples before and after simulated irradiation. An IKS-29 IR spectrophotometer (LOMO) was used to record absorption spectra in the IR range.

The IR spectra of the SK45-Pb10 glass matrix sample before and after irradiation with X-rays up to an absorbed dose of 10 and 100 kGy are shown in Fig. 6 and 7. Before irradiation, the IR spectrum of the SK45- Pb10 glass matrix has a broad band in the region of 470 cm^{-1} and a broad doublet band with weak maxima at 980 and 1020 cm^{-1}. These bands refer, respectively, to the bending and stretching vibrations of O-Si-O in the silicon-oxygen glass network. The spectrum shows a weak peak at 700 cm^{-1} associated with symmetric stretching vibrations of the Si-O-Si bridges, as well as a peak at 1590 cm^{-1} (deformation vibrations of OH in water molecules) and a doublet at 3400 and 3450 cm^{-1}, caused by the presence of two types of H_2O: structurally bound and absorbed (Table 4).
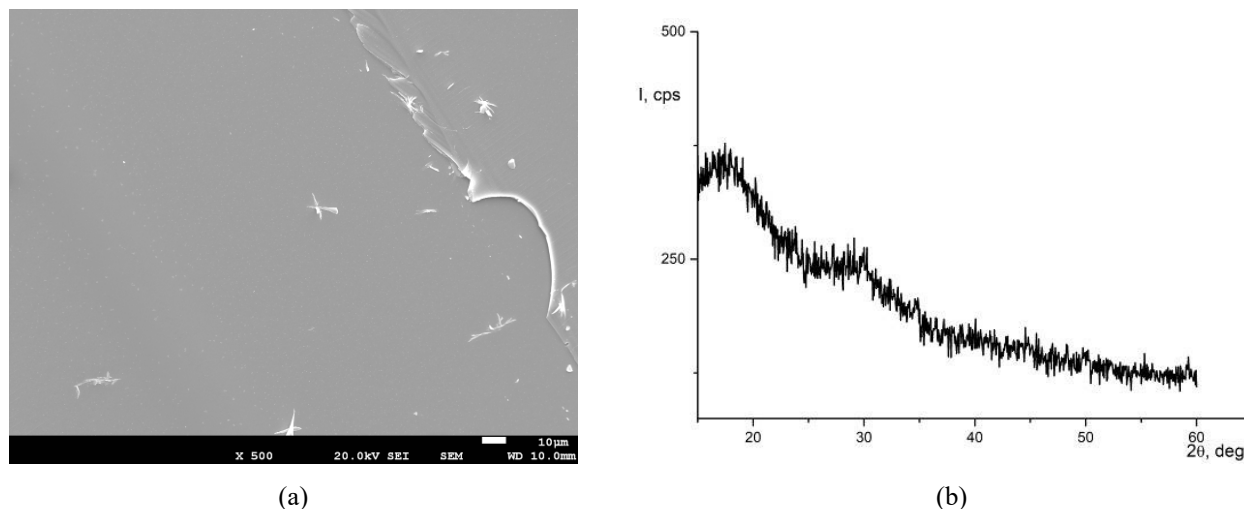

(a)   (b)

Figure 5. Structure and phase composition of SK45-Pb10 glass matrix samples after irradiation
a – SEM image, b – diffraction pattern.

As a result of irradiation to an absorbed dose of 10 kGy, the intensity of the main bands associated with Si-O-Si vibrations decreases, and their shift to the low-frequency region is observed due to a decrease in the degree of coupling of the silicon-oxygen framework. The bands of both structurally bound and adsorbed water completely disappear. When the dose is increased to 100 kGy, no significant changes in the spectrum occur, except for the appearance of a weak band of adsorbed water in the region of 3360 cm^{-1}.
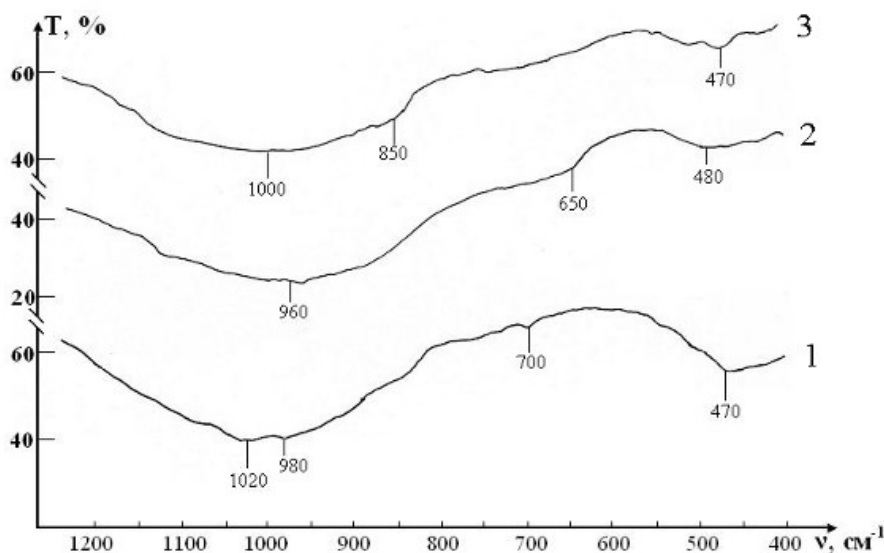

Figure 6. IR absorption spectra of SK45-Pb10 glass samples in the range 400-1200 cm^{-1}
1- before irradiation, 2- irradiation (10 kGy), 3- irradiation (100 kGy)

The IR absorption spectra of the SK45-CF10 glass in the initial state and after irradiation with X-rays up to 10 kGy are shown in Figs. 8 and 9. In the spectrum of the original glass, there are a number of broad bands with diffuse maxima due to bending and stretching vibrations of the Si-O bonds (Table 5). The presence of a weak peak at 3390 cm^{-1} in the spectrum indicates that the initial glass contains a small amount of adsorbed water.

As a result of irradiation with a dose of 10 kGy, the shape and intensity of the main bands in the IR spectrum does not change, but the appearance of a low-frequency shoulder (940 cm^{-1}) on the band in the region of 1000 cm^{-1} is noted.

This indicates the beginning of depolymerization of the silicon-oxygen network [8]. In addition, the occurrence of an inflection in the region of 1350 cm^{-1} indicates the formation of some amount of boron in triple coordination.

Thus, according to the data of IR spectroscopy, as a result of X-ray irradiation of SK45-Pb10 glass to a dose of 10 kGy, the degree of bonding of the silicon-oxygen skeleton of the glass begins to decrease and both structurally bound and adsorbed water are lost. When the dose is increased to 100 kGy, no significant changes occur. Irradiation of SK45-CF10 glass up to 10 kGy leads to the onset of depolymerization of the silicon-oxygen network of the glass and the formation of boron in triple coordination. However, the detected minor changes in the IR spectra do not affect the composition, structure and chemical bonds of the obtained glass matrices, and, accordingly, their insulating properties. That is, the resulting SK45-Pb10 and SK45-CF10 glass matrices have sufficient radiation resistance, which can ensure its integrity and stability during long-term storage.
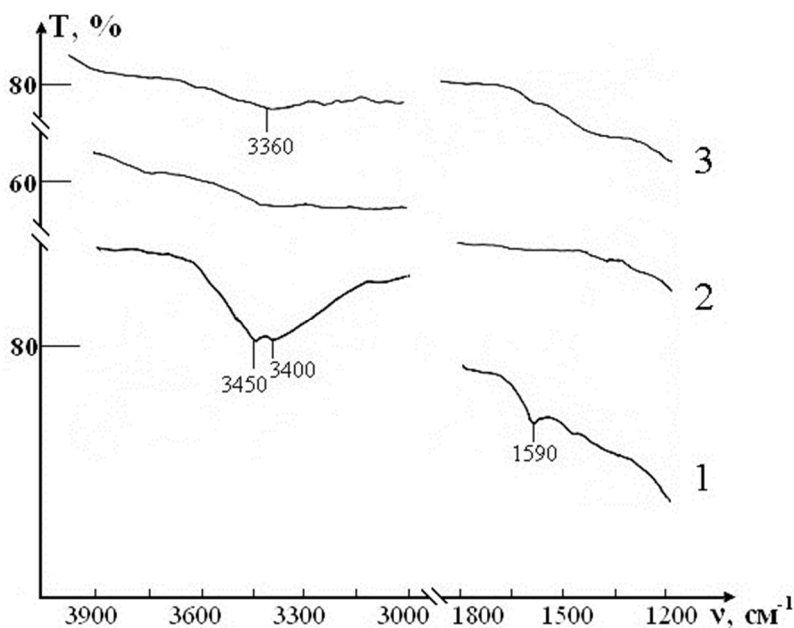

Figure 7. IR absorption spectra of SK45-Pb10 glass samples in the range 1200-4000 cm^{-1}
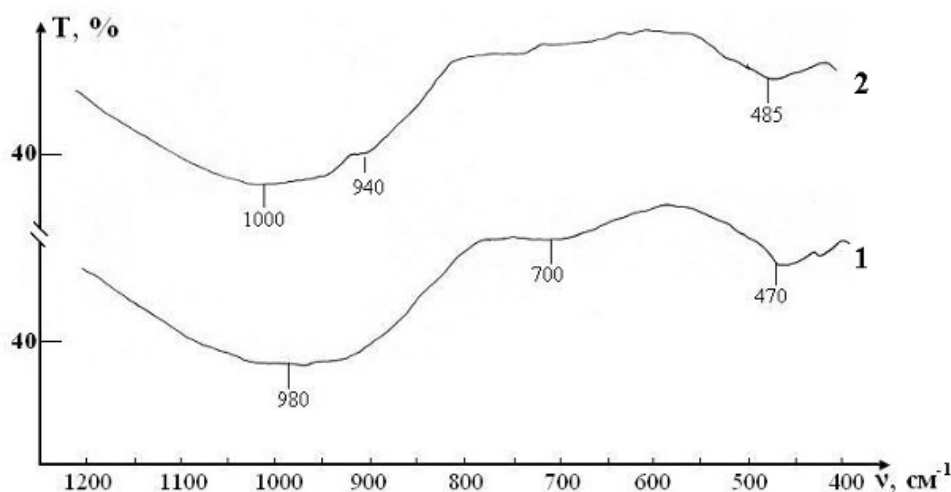1- before irradiation, 2-irradiation (10 kGy), 3-irradiation (100 kGy)

Figure 8. IR absorption spectra of SK45-CF10 glass samples in the range 400-1200cm^{-1}
1 – before irradiation, 2 – Irradiation (10 kGy)

CONCLUSION

Radiation testing of glass matrix samples was carried out using simulated X-ray irradiation at the linear electron accelerator LU-10 (KIPT). It is shown that the material of the obtained glass matrices retains its integrity and amorphous structure after irradiation with X rays up to an absorbed dose of 10 KGy and 100KGy. According to IR spectrometry, as a result of irradiation of samples of glass matrices to an absorbed dose of 10 kGy, there is an

insignificant decrease in the degree of bonding of the silicon–oxygen framework of the glass. When the dose is increased to 100 kGy, no significant changes occur.

The resulting lead-borosilicate glass matrix, which is characterized by high radiation resistance and includes the maximum amount of radioactive waste simulator - up to 45 wt.%, can be used for effective fixation of bottom residues of NPP LRW.

Table 4. Assignment of bands in the spectra of glass matrix samples SK45-Pb10

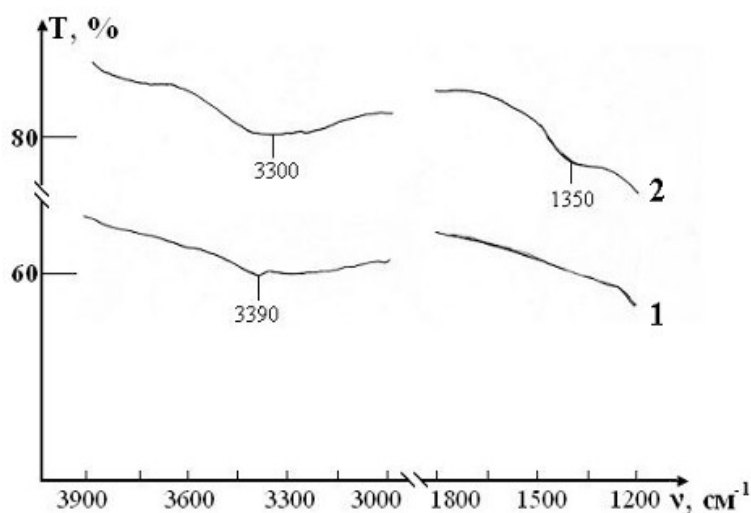| Before exposure	Irradiation D=10 kGy	Irradiation D=100 kGy	Band assignment [8, 9]
470	480	470	Deformation vibrations of the Si-O-Si bond in tetrahedra SiO_4^{4-}
700	-	-	Symmetric stretching vibrations of Si-O-Si bridges
980, 1020	960	850, 1000	Stretching vibrations of the Si-O-Si bond in tetrahedra SiO_4^{4-}
1590	-	-	Bending vibrations of the OH bond in water molecules
3400, 3450	-	3360	Stretching vibrations of the OH bond in water molecules

Figure 9. IR absorption spectra of SK45-CF10 glass samples in the range 1200-4000 cm^{-1}
1 – before irradiation, 2 – Irradiation (10 kGy).

Table 5. Assignment of bands in the spectra of glass matrix samples SK45-Pb10

Before exposure	Irradiation D=10 kGy	Band assignment [8, 9]
470	485	Deformation vibrations of the Si- O-Si bond in tetrahedra SiO_4^{4-}
700	-	Symmetric stretching vibrations of Si-O-Si bridges
980	940, 1000	Stretching vibrations of the Si-O- Si bond in tetrahedra SiO_4^{4-}
–	1350	Boron in triple coordination in groups BO_3
3390	3300	Stretching vibrations of the OH bond in water molecules

A code was developed for calculating absorbed doses over 300 years in lead-borosilicate glass (chemical composition is given in Table 3) for isotopes ^{137}Cs, ^{134}Cs, ^{60}Co for the GEANT4 software package. The calculated absorbed dose received by 200-liter cylinder of lead-borosilicate glass is equal to 627.9 Gy. Main absorbed dose in the sample accumulates over the first 150 years.

ORCID IDs
Volodymyr Morgunov, https://orcid.org/0000-0002-8681-1941; **Sergii Sayenko,** https://orcid.org/0000-0002-2598-3598
Volodymyr Shkuropatenko, https://orcid.org/0000-0003-2618-0858; **Yevhenii Svitlychnyi,** https://orcid.org/0000-0002-6522-4940
Olena Bereznyak, https://orcid.org/0000-0003-2126-346X; **Serhii Lytovchenko,** https://orcid.org/0000-0002-3292-5468
Volodymyr Chyshkala, https://orcid.org/0000-0002-8634-4212

REFERENCES
[1] S.Y. Sayenko, V. Shkuropatenko, A. Pylypenko, A. Zykova, S. Karsim, V. Andrieieva, and S. Moshta, PAST, **2**, 103 (2020), https://vant.kipt.kharkov.ua/ARTICLE/VANT_2020_2/article_2020_2_103.pdf.
[2] N. Laverov, B. Omelchenko, S. Udincev, S. Stefanovskii, and B. Nikonov, Геология рудных месторождений [Geology of ore deposits], **55**, 87 (2013). (in Russian)
[3] M. Ozhovan, and P. Poluektov, Priroda—Nature, 3–11 (2010).
[4] S. Luo, J. Sheng, and B. Tang, Journal of nuclear materials, **298**, 180 (2001), https://doi.org/10.1016/S0022-3115(01)00592-X.
[5] S. Agostinelli, J. Allison, K. Amako, J. Apostolakis, H. Araujo, P. Arce, M. Asai, et al, Nuclear Instruments and Methods in Physics Research Section A: Accelerators, Spectrometers, Detectors and Associated Equipment, **506**, 250 (2003), https://doi.org/10.1016/S0168-9002(03)01368-8.
[6] J. Allison, K. Amako, J. Apostolakis, H. Araujo, P. Arce Dubois, M. Asai, G. Barrand, et al, IEEE Transactions on Nuclear Science, **53**, 270 (2006). https://doi.org/10.1109/TNS.2006.869826.
[7] J. Allison, K. Amako, J. Apostolakis, P. Arce, M. Asai, T. Aso, E. Bagli, and et al, Nuclear Instruments and Methods in Physics Research Section A: Accelerators, Spectrometers, Detectors and Associated Equipment, **835**, 186 (2016). https://doi.org/10.1016/j.nima.2016.06.125.
[8] S.V. Stefanovskii, The Soviet Journal of Glass Physics and Chemistry, **16** (1991). (in Russian)
[9] S. Stefanovskii, I. Ivanov, A. Gulin, and F. Lifanov, Radiokhimiya, **35**, 106 (1993). (in Russian)

РОЗРАХУНОК ПОГЛИНЕНОЇ ДОЗИ МАТРИЦЕЮ БОРОСИЛІКАТНОГО СКЛА ТА ЇЇ МОДЕЛЬНЕ ОПРОМІНЮВАННЯ

В.В. Моргунов[a], С.Ю. Саенко[b], В.А. Шкуропатенко[b], Є.О. Світличний[b], О.П. Березняк[b], С.В. Литовченко[a], В.О. Чишкала[a]

[a]*Харківський національний університет імена В. Н. Каразіна, м. Свободи, 4, Харків, 61022, Україна;*

[b]*Національний науковий центр "Харківський фізико - технічний інститут вул. Академічна, 1, Харків, 61108, Україна*

Стан поводження з рідкими радіоактивними відходами (РРВ) на АЕС України характеризується відсутністю завершеного технологічного циклу від переробки до отримання кінцевого продукту, придатного для подальшого тривалого зберігання або захоронення. В результаті резервуари для донного залишку (ДЗ) заповнені на 65-75% (Запорізька та Південно-Українська АЕС), а ресурс розміщення соляного розплаву на Запорізькій АЕС (92,7%) близький до вичерпання. Тому розробка технологій і матеріалів для затвердіння РРВ АЕС є актуальною і спрямована на забезпечення переробки РРВ до твердого стану, який відповідатиме критеріям прийнятності для захоронення в централізованих сховищах. Одним із ефективних методів затвердіння РРВ є їх осклування. Основна перевага вітрифікації полягає в тому, що під час процесу вітрифікації об'єм відходів зменшується в кілька разів, що економить дороге місце для зберігання. Метою цієї роботи є розрахунок поглиненої дози, яку накопичують матриці з боросилікатного скла з доданим донним залишком протягом 300 років зберігання, а також дослідження впливу імітованого рентгенівського опромінення на їхні фізико-механічні властивості.

Ключові слова: рідинні радіоактивні відходи, кубовий залишок, матриця з боросилікатного скла, поглинена доза, чисельне моделювання.

EFFECTS OF GRAVITATIONAL FIELD OF A TOPOLOGICAL DEFECT ON STATISTICAL PROPERTIES OF HEAVY QUARK-ANTIQUARK SYSTEMS[†]

André Aimé Atangana Likéné[a,c,*], Ali Zarma[a], Dieudonné Nga Ongodo[a,†],
Jean Marie Ema'a Ema'a[b,#], Patrice Ele Abiama[a,c,§], Germain Hubert Ben-Bolie[a,‡]

[a]Laboratory of Atomic, Molecular and Nuclear Physics, Department of Physics, Faculty of Science
University of Yaounde I, P.O. Box 812, Yaounde, Cameroon
[b]Ngaoundere Higher Teachers' Training College, Department of Physics, University of Maroua
P.O. Box 55, Bertoua, Cameroon
[c]The Nuclear Technology Section (NTS), Institute of Geological and Mining Research
P.O. Box 4110, Yaounde, Cameroon
*Corresponding Autor: aandreaime@yahoo.fr. Phone (Direct):+237-9742-7891
[†]E-mail: ngadieudonne@yahoo.fr; [#]E-mail: emaaejm@yahoo.fr; [§]E-mail: eleabiama2003@yahoo.fr, [‡]E-mail: gbenbolie@yahoo.fr

In this paper, we determine eigen energies, eigenfunctions and statistical properties of non-relativistic heavy quarkonia interacting with the extended Cornel potential within a space-time generated by a cosmic-string. We extend the Cornel potential by adding the inverse square potential plus the quadratic potential. We have calculated the energy eigenvalues and the corresponding eigenstates using the Extended Nikiforov-Uvarov (ENU) method. Then, based on the equation of energy spectra, the thermodynamic properties like partition function, entropy, free energy, mean energy and specific heat capacity are calculated within the space-time of a cosmic-string. In the next step, we investigate the influence of the cosmic-string parameter on quantum states of heavy quarkonia and their statistical properties.
Keywords: thermodynamic properties, quark, Schrödinger wave equation, topological defect, space-time, cosmic string, extended Cornel potential, meson, extended Nikiforov-Uvarov method.
PACS: 12.39.Jh, 12.39.Pn, 14.40.Pq, 03.65.Ge

1. INTRODUCTION

The study of quantum particles under the influence of a potential in a curved space-time with Topological defect has inspired a large number of research in recent years [1, 2, 3, 4, 5, 6] with different motivations. Kibble [4, 5] was the first to state the mechanism which would have led to the appearance of topological defects in the universe. According to grand unification theories (GUT) [4, 5, 6], the conditions which reigned in the very early moments of the universe were such that the four fundamental interactions were one [4, 5, 7]. A few moments after the Big-Bang, the universe began to expand and became less and less hot and its density decreased [7, 8]. From the initial phase where the grand unification symmetries would be realized, a spontaneous breaking of these symmetries would then have taken place and at this moment, stable topological defects were formed.

Thus, a large variety of topological defects have been studied in previous works, namely: point defects [4, 5, 6, 7, 8] called monopoles, linear defects or cosmic-strings [4, 5, 7], surface defects or "domain walls" [9], and also combinations between these different defects [10, 11, 12]. These faults are often stable; so, it is absolutely possible that some of them would have survived, until now [9]. However, cosmic strings are compatible with cosmological models [6] and current observations. Their cosmological effects could be confirmed with current and future work. It is therefore quite logical to give particular interest to the study of quantum systems on curved space-time with cosmic-string background. In [6], the author presents cosmic-strings as the most important topological defect in our universe.

Their effects on the environment are mainly gravitational in nature [6, 10, 11, 12]. To this end, a quantum particle placed in a gravitational field will be influenced by the topology of the space and by its interaction with the local curvature. From this interaction, it follows that an observer at rest with respect to the particle will see a shift in its spectrum. This would be of considerable interest both from a theoretical and an observational point of view. Apart from the effects due to the gravitational field, other effects can be induced by a cosmic-string, like for example bremsstrahlung process [13], the creation of the (e^+, e^-) pair [14], gravitational leasing [15] and the gravitational Aharonov-Bohm effect [16].

The study of thermodynamic properties of quantum systems plays a major role in theoretical High Energy Physics (HEP) and related fields [17]. Usually, quarks and gluons remain confined in hadrons and in particular in the protons and neutrons which form the atomic nucleus. Indeed, Quantum Chromodynamics (QCD), a theory that accounts for the strong interaction predicts that by compressing or heating nuclei, it is possible to create a plasma of quarks and gluons [18, 19], a matter with poorly understood thermodynamic properties. In past few decades, some experimental works have been carry out to identify the existence of deconfinement transitions [19] and determine its signatures. Then, it was predicted

that the suppression of charmonium (*a bound state of charm and anti-charm quarks*) meson is a possible signature of the QCD phase transition [18, 19, 20]. This phenomenon of deconfining matter is in principle observable through the study of the **J**/ψ particle [20], a meson as heavy as three surrounding protons. The suppression of the $c\bar{c}$ meson has been announced as being the signature of deconfinement transition, it would be interesting to study in depth the thermodynamic properties of heavy mesons, in this case heavy quarkonia.

In [21], the author obtained thermodynamic properties of the quark-gluon plasma from the constituent quasi particle model of quark-gluon plasma. Then in [22, 23, 24], thermodynamic properties are investigated using chiral quark models. In this work, we obtain the solutions of the Schrödinger equation produced by the gravitational field of a topological defect, for all values of the orbital angular momentum quantum number l. The Extended Nikiforov-Uvarov method [25, 26] is used to obtain exact analytical solutions of the radial Schrödinger equation in cosmic-string background. Next, we apply the results to obtain the thermodynamic properties of heavy quarkonia from cosmic-string geometry, which is not consider in other works.

This paper is organized as follows: in Section 2, the Extended Nikiforov-Uvarov method is reviewed. The bound state solutions for the extended Cornel potential are obtained for the Schrödinger equation in cosmic-string background in Section 3. Then in section 4, thermodynamic properties of heavy quarkonia within cosmic-string geometry are presented. In Section 5 results are discussed, and conclusions are presented in Section 6.

2. BASIC CONCEPTS OF THE EXTENDED NIKIFOROV-UVAROV METHOD

In this section, we briey present the Extended Nikiforov-Uvarov (ENU) technique, for more details see [25, 26, 27]. The extended Nikiforov-Uvarov method is obtained by changing the boundary conditions of the standard Nikiforov-Uvarov (NU) method and is used for solving any second order differential equation which has at most four singular points. The equation to be solved is of the form:

$$\psi''(r) + \frac{\bar{\tau}(r)}{\sigma(r)}\psi'(r) + \frac{\bar{\sigma}(r)}{\sigma^2(r)}\psi(r) = 0, \tag{1}$$

such that $\bar{\tau}(r)$, $\sigma(r)$ and $\bar{\sigma}(r)$ are polynomials of at most second, third and fourth degree, respectively. By choosing ψ such that:

$$\psi(r) = \phi(r)Y(r), \tag{2}$$

where $\phi(r)$ and $Y(r)$ are functions to be determined later. Moreover, considering the above substitution Eq. (1) reduces to an equation of the form

$$\sigma(r)Y''(r) + \tau(r)Y'(r) + h(r)Y(r) = 0, \tag{3}$$

where $\phi(r)$ solves the equation

$$\frac{\phi'(r)}{\phi(r)} = \frac{\pi(r)}{\sigma(r)}, \tag{4}$$

$$h(r) - \pi'(r) = G(r). \tag{5}$$

And the polynomials of the function $Y(r)$ satisfy the Rodriguez formula [27]

$$Y_n(r) = \frac{B_n}{\rho(r)}\frac{d^n}{dr^n}\left[\sigma^n(r)\rho(r)\right]. \tag{6}$$

In Eq. (6), B_n is the normalization factor and ρ is the density function. The function ρ solves the following equation:

$$\left(\sigma(r)\rho(r)\right)' = \tau(r)\rho(r). \tag{7}$$

The function $\pi(r)$ required for this method are given by:

$$\pi(r) = \frac{\sigma'(r) - \bar{\tau}(r)}{2} \pm \sqrt{\left(\frac{\sigma'(r) - \bar{\tau}(r)}{2}\right)^2 - \bar{\sigma}(r) + G(r)\sigma(r)}, \tag{8}$$

where $\pi(r)$ is a second-degree polynomial. The function $h_n(r)$ is determined from the equation

$$h_n(r) = -\frac{n}{2}\tau'(r) - \frac{n(n-1)}{6}\sigma''(r) + C_n, \tag{9}$$

where $\tau(r) = \overline{\tau}(r) + 2\pi(r)$ and C_n is an integration constant. In the order to obtain the eigenvalue solution of the problem by ENU method [25, 26, 27], the polynomials $h(r)$ and $h_n(r)$ are equal and $Y(r) = Y_n(r)$ is a particular solution of degree n of Eq. (3). The function $\phi(r)$ is defined as a logarithmic derivative given in Eq. (4), and then eigenfunction spectra can be obtained analytically. For more details one can see Refs. [26] and [27].

3. SCHRÖDINGER WAVE EQUATION IN THE SPACE-TIME OF A COSMIC STRING

In spherical coordinates, the line element describing the cosmic string space-time [6] is given by $\left(x^0 = ct,\ x^1 = r,\ x^2 = \theta,\ x^3 = \varphi\right)$

$$ds^2 = g_{\mu\nu}dx^\mu \otimes dx^\nu = -c^2 dt^2 + dr^2 + r^2 d\theta^2 + \left[\chi d\theta + \alpha r \sin\theta d\varphi\right]^2, \tag{10}$$

where $0 < r < \infty$, $0 < \theta < \pi$, and $0 < \varphi < 2\pi$, $0 < \alpha = 1 - 4J$ is the topological parameter of the cosmic string, $\chi = \frac{4GJ}{c^3}$, is the torsion [23] parameter and J denotes the linear mass density [28, 29,30,31] of the cosmic string. From General Relativity (GR), we know that the values of J varies in the interval $J \in]0,1[$.

For $\alpha \to 1$ and $\chi \to 0$, the metric given by Eq. (10) reduces to the usual Minkowski metric in spherical coordinates. The metric tensor for the space-time described by Eq. (10) is:

$$g_{\mu\nu}(x) = \begin{pmatrix} -1 & 0 & 0 & 0 \\ 0 & 1 & 0 & 0 \\ 0 & 0 & \chi^2 + r^2 & \chi\alpha r\sin\theta \\ 0 & 0 & \chi\alpha r\sin\theta & \alpha^2 r^2 \sin^2\theta \end{pmatrix} = \begin{bmatrix} -1 & 0 \\ 0 & \left(g_{ij}\right) \end{bmatrix}, \tag{11}$$

with the inverse metric,

$$g^{\mu\nu}(x) = \begin{pmatrix} -1 & 0 & 0 & 0 \\ 0 & 1 & 0 & 0 \\ 0 & 0 & \dfrac{1}{r^2} & -\dfrac{\chi}{\alpha r^3 \sin\theta} \\ 0 & 0 & -\dfrac{\chi}{\alpha r^3 \sin\theta} & \dfrac{\chi^2 + r^2}{\alpha^2 r^4 \sin^2\theta} \end{pmatrix}, \tag{12}$$

We adopt the signature $(-,+,+,+)$ for the metric tensor $g^{\mu\nu}$, and its determinant is given by $g = det\left(g^{\mu\nu}\right) = -\alpha^2 r^4 \sin^2\theta$, with $\mu,\nu = 0,1,2,3$. In the curvilinear coordinates system $ds^2 = \sum_{i=1}^3 \sum_{j=1}^3 g_{ij} dx^i \otimes dx^j$ such that $r \to x^1$, $\theta \to x^2$, $\varphi \to x^3$ the metric tensor of the internal 3-dimensional Euclidian space is:

$$g_{ij}(x) = \begin{pmatrix} 1 & 0 & 0 \\ 0 & \chi^2 + r^2 & \chi\alpha r\sin\theta \\ 0 & \chi\alpha r\sin\theta & \alpha^2 r^2 \sin^2\theta \end{pmatrix}. \tag{13}$$

The Laplace-Beltrami operator of the local coordinates system can be expressed as:

$$\Delta_{LB} = \frac{1}{\sqrt{g}}\frac{\partial}{\partial x^i}\left(g^{ij}\sqrt{g}\frac{\partial}{\partial x^i}\right) \qquad i,j = 1,2,3 \qquad \text{and} \quad g = det\left(g_{ij}\right) = \alpha^2 r^4 \sin^2\theta. \tag{14}$$

Then, considering Eq. (14) and for small values of the torsion parameter $\chi \ll 1$, the Laplace-Beltrami operator becomes:

$$\Delta_{LB} = \frac{1}{r^2}\left\{\frac{\partial}{\partial r}\left[r^2\left(\frac{\partial}{\partial r}\right)\right]\right\} + \cot\theta\frac{\partial}{\partial\theta} + \frac{\partial^2}{\partial\theta^2} + \frac{1}{\alpha^2 \sin^2\theta}\frac{\partial^2}{\partial\varphi^2}, \tag{15}$$

from this we can write the Hamiltonian operator in natural units ($\hbar = c = 1$) as:

$$H = -\frac{1}{2M}\left[\frac{\partial^2}{\partial r^2} + \frac{2}{r}\frac{\partial}{\partial r} + \frac{1}{r^2}\cot\theta\frac{\partial}{\partial\theta} + \frac{1}{r^2}\frac{\partial^2}{\partial\theta^2} + \frac{1}{r^2}\frac{1}{\alpha^2\sin^2\theta}\frac{\partial^2}{\partial\varphi^2}\right] + V(r,\theta,\varphi),\tag{16}$$

$M = m_q m_{\bar{q}} / (m_q + m_{\bar{q}})$ is the reduced mass of the quark-antiquark system, where m_q and $m_{\bar{q}}$ are the mass of quark and antiquark respectively [8, 26].

The non-relativistic Schrödinger equation in curved background space-time is [16, 23]

$$i\hbar\frac{\partial}{\partial t}\Psi(\vec{r},t) = -\frac{\hbar^2}{2M}\left[\frac{\partial^2}{\partial r^2} + \frac{2}{r}\frac{\partial}{\partial r} + \frac{1}{r^2}\cot\theta\frac{\partial}{\partial\theta} + \frac{1}{r^2}\frac{\partial^2}{\partial\theta^2} + \frac{1}{r^2}\frac{1}{\alpha^2\sin^2\theta}\frac{\partial^2}{\partial\varphi^2}\right]\Psi(\vec{r},t) + V(\vec{r})\Psi(\vec{r},t),\tag{17}$$

here, we consider bound states of two heavy quarks interacting with the extended Cornel potential [26, 32]

$$V(r) = -\frac{K}{r} + \alpha r + \frac{g}{r^2} + br^2.\tag{18}$$

The first term is a Coulomb-like potential due to one-gluon exchange processes between quark-antiquark [32], the second term is a linear confinement term. The additional part was added to improve quark-antiquark properties [26, 32, 33]. As $V = V(r)$, the following commutation relations must be satisfied

$$\left[L_z, V(r)\right] = 0, \qquad \left[L^2, V(r)\right] = 0.\tag{19}$$

Consequently, L_z and L^2 are good quantum numbers to describe the quantum states of the system under the influence of this potential. Inserting the new form of Ψ as

$$\Psi(\vec{r},t) = \frac{\psi_{nl}(r)}{r}H_l^m(\theta)\Phi_m(\varphi)e^{-iE_{nl}t},\tag{20}$$

and substituting in Eq. (17) gives the following set of second-order differential equations,

$$\frac{d^2\psi_{nl}(r)}{dr^2} + \left[-\frac{2M}{\hbar^2}V(r) + \frac{2M}{\hbar^2}E_{nl} - \frac{\delta}{r^2}\right]\psi_{nl}(r) = 0,\tag{21}$$

$$\frac{d^2H_l^m(\theta)}{d\theta^2} + \cot\theta\frac{dH_l^m(\theta)}{d\theta} + \left[\delta - \frac{m^2}{\alpha^2\sin^2\theta}\right]H_l^m(\theta) = 0,\tag{22}$$

$$\frac{d^2\Phi_m(\varphi)}{d\varphi^2} + m^2\Phi_m(\varphi) = 0,\tag{23}$$

where δ and m^2 are the separation constants. Using the following boundary condition: $\Phi_m(\varphi + 2\pi) = \Phi_m(\varphi)$, we can easily obtain the solution of Eq. (23) as

$$\Phi_m(\varphi) = \frac{1}{\sqrt{2\pi}}e^{im\varphi}, \qquad m = 0, \pm 1, \pm 2, \pm 3,\dots.\tag{24}$$

To find the solutions of Eq. (22), we introduce the variable $\eta = \cos\theta$, which map Eq. (22) into

$$\frac{d^2H_l^m(\eta)}{d\eta^2} - \frac{2\eta}{(1-\eta^2)}\frac{dH_l^m(\eta)}{d\eta} + \left[\delta - \frac{m^2}{\alpha^2(1-\eta^2)}\right]H_l^m(\eta) = 0.\tag{25}$$

To obtain suitable solutions of Eq. (25), it is therefore necessary to analyze the way the solutions behave around singular points, namely $\pm\eta$. Then we assume the following form for the solution:

$$H_l^m(\eta) = (1-\eta^2)^{\frac{m}{2\alpha}}g_l(\eta),\tag{26}$$

where g_l is analytic everywhere except at $\eta \to \pm \infty$. From Eq. (25) and Eq. (26), and introducing the following generalized quantum numbers, namely $l_{(\alpha)}$, $m_{(\alpha)} = \dfrac{m}{\alpha}$, from the cosmic-string geometry, we obtain the following equation:

$$\left(1-\eta^2\right)\frac{d^2 g_{l(\alpha)}(\eta)}{d\eta^2} - 2\left(m_{(\alpha)}+1\right)\eta\frac{d g_{l(\alpha)}(\eta)}{d\eta} - \left[m^2_{(\alpha)} + m_{(\alpha)} - \delta\right]g_{l(\alpha)}(\eta). \tag{27}$$

From the expansion of $g_{l(\alpha)}(\eta)$ into a power series,

$$g_{l(\alpha)}(\eta) = \sum_{-\infty}^{+\infty} a_n \eta^n, \tag{28}$$

and inserting in Eq. (27) gives us the following recurrence relation:

$$a_{n+2} = \frac{n(n-1) + 2\left(m_{(\alpha)}+1\right)n - \delta + m_{(\alpha)}\left(m_{(\alpha)}+1\right)}{(n+1)(n+2)} a_n, \tag{29}$$

where $n = 0, 1, 2, 3, \dots$. For physically acceptable solutions, the series must be truncated at a certain value of n:

$$n(n-1) + m_{(\alpha)}\left(m_{(\alpha)}+1\right) + 2\left(m_{(\alpha)}+1\right)n - \delta = 0. \tag{30}$$

Solving for δ gives:

$$\delta = l_{(\alpha)}\left(l_{(\alpha)}+1\right) \quad \text{with} \quad l_{(\alpha)} = m_{(\alpha)} + n, \tag{31}$$

$l_{(\alpha)}$ being the generalized angular orbital quantum number. The generalized quantum numbers $l_{(\alpha)}$ and $m_{(\alpha)}$ are not always integers. $l_{(\alpha)} = m_{(\alpha)} + n = \dfrac{m}{\alpha} + n = l - \left(l - \dfrac{1}{\alpha}\right)m$, where $l = 0, 1, 2, \dots$ Eq. (25) can therefore take the form:

$$\left(1-\eta^2\right)\frac{d^2 H^{m_{(\alpha)}}_{l(\alpha)}(\eta)}{d\eta^2} - 2\eta\frac{d H^{m_{(\alpha)}}_{l(\alpha)}(\eta)}{d\eta} + \left[l_{(\alpha)}\left(l_{(\alpha)}+1\right) - \frac{\left[m_{(\alpha)}\right]^2}{\left(1-\eta^2\right)}\right]H^{m_{(\alpha)}}_{l(\alpha)}(\eta), \tag{32}$$

where Eq. (32) is the generalized Legendre equation within the cosmic-string space-time and $H^{m_{(\alpha)}}_{l(\alpha)}(\eta)$ are the generalized Legendre polynomials given by the formula:

$$H^{m_{(\alpha)}}_{l(\alpha)}(\eta) = P^{m_{(\alpha)}}_{l(\alpha)}(\eta) = \frac{(-1)^{l(\alpha)}}{2^{l(\alpha)} l_{(\alpha)}!}(1-\eta)^{\frac{m_{(\alpha)}}{2}}\frac{d^{l(\alpha)+m_{(\alpha)}}}{d\eta^{l(\alpha)+m_{(\alpha)}}}\left[\left(1-\eta^2\right)^{l(\alpha)}\right]. \tag{33}$$

Let's now turn to the radial equation.

Substituting the proposed potential in Eq. (21) and choosing the separation constant being $\delta = l_{(\alpha)}\left(l_{(\alpha)}+1\right)$, the radial equation becomes:

$$\frac{d^2 \psi_{nl}(r)}{dr^2} + \frac{1}{r^2}\left[-2Mg - l_{(\alpha)}\left(l_{(\alpha)}+1\right) + 2MKr + 2M\left(E_{nl} - d\right)r^2 - 2Mar^3 - 2Mbr^4\right]\psi_{nl}(r) = 0, \tag{34}$$

that we put in a simple form by introducing the following constants:

$$\begin{aligned} \xi_0 &= l_{(\alpha)}\left(l_{(\alpha)}+1\right) + 2Mg, \quad \xi_1 = 2MK, \quad \xi_2 = 2M\left(E_{nl} - d\right) \\ \xi_3 &= 2Ma, \quad \xi_4 = 2Mb \end{aligned}. \tag{35}$$

The functions from the Nikiforov-Uvarov method are:

$$\bar{\tau}(r) = 0, \tag{36}$$

$$\sigma(r) = r^2, \tag{37}$$

$$\overline{\sigma}(r) = -\xi_0 + \xi_1 r + \xi_2 r^2 - \xi_3 r^3 - \xi_4 r^4. \tag{38}$$

Using equation Eq. (10), $\pi(r)$ is found as:

$$\pi(r) = \frac{1}{2} \pm \sqrt{\xi_0 + \frac{1}{4} - \xi_1 r - \xi_2 r^2 + \xi_3 r^3 + \xi_4 r^4 + rG(r)}. \tag{39}$$

Assuming that the term under the square root of the above expression becomes quadratic,

$$\pi(r) = \frac{1}{2} \pm (\alpha_0 + \alpha_1 r + \alpha_2 r^2). \tag{40}$$

Let's take the function $G(r)$ in the form $G(r) = Ar + B$. By comparison between Eq. (39) and Eq. (40), we obtain the following four sets of solutions for the unknowns α_2, α_1, α_0 A and B in terms of the problem parameters:

$$
\mathbf{I}: \begin{cases}
\alpha_2 = \sqrt{\xi_4} \\
\alpha_1 = \dfrac{\xi_3}{2\sqrt{\xi_4}} \\
\alpha_0 = \sqrt{\xi_0 + \dfrac{1}{4}} \\
A = \xi_2 + \dfrac{[\xi_3]^2}{4\sqrt{\xi_4}} + 2\sqrt{\xi_4}\sqrt{\xi_0 + \dfrac{1}{4}} \\
B = \xi_1 + \dfrac{\xi_3}{\sqrt{\xi_4}}\sqrt{\xi_0 + \dfrac{1}{4}}
\end{cases}
\qquad
\mathbf{II}: \begin{cases}
\alpha_2 = -\sqrt{\xi_4} \\
\alpha_1 = -\dfrac{\xi_3}{2\sqrt{\xi_4}} \\
\alpha_0 = \sqrt{\xi_0 + \dfrac{1}{4}} \\
A = \xi_2 + \dfrac{[\xi_3]^2}{4\sqrt{\xi_4}} - 2\sqrt{\xi_4}\sqrt{\xi_0 + \dfrac{1}{4}} \\
B = \xi_1 - \dfrac{\xi_3}{\sqrt{\xi_4}}\sqrt{\xi_0 + \dfrac{1}{4}}
\end{cases}
$$

$$
\mathbf{III}: \begin{cases}
\alpha_2 = \sqrt{\xi_4} \\
\alpha_1 = \dfrac{\xi_3}{2\sqrt{\xi_4}} \\
\alpha_0 = -\sqrt{\xi_0 + \dfrac{1}{4}} \\
A = \xi_2 + \dfrac{[\xi_3]^2}{4\sqrt{\xi_4}} - 2\sqrt{\xi_4}\sqrt{\xi_0 + \dfrac{1}{4}} \\
B = \xi_1 - \dfrac{\xi_3}{\sqrt{\xi_4}}\sqrt{\xi_0 + \dfrac{1}{4}}
\end{cases}
\qquad
\mathbf{IV}: \begin{cases}
\alpha_2 = -\sqrt{\xi_4} \\
\alpha_1 = -\dfrac{\xi_3}{2\sqrt{\xi_4}} \\
\alpha_0 = -\sqrt{\xi_0 + \dfrac{1}{4}} \\
A = \xi_2 + \dfrac{[\xi_3]^2}{4\sqrt{\xi_4}} + 2\sqrt{\xi_4}\sqrt{\xi_0 + \dfrac{1}{4}} \\
B = \xi_1 + \dfrac{\xi_3}{\sqrt{\xi_4}}\sqrt{\xi_0 + \dfrac{1}{4}}
\end{cases}
\tag{41}
$$

Considering Eq. (4), we have two solutions for $\phi(r)$ which are given by:

$$\phi_\pm(r) = K_\pm r^{\frac{1}{2} \mp \alpha_0} \exp\left(\pm \frac{1}{2}(\alpha_2 r^2 + 2\alpha_1 r) \right). \tag{42}$$

The wave function will be physically acceptable if $\alpha_1 < 0$, $\alpha_2 < 0$ and $\alpha_0 > 0$ and then the set **II** of parameters is the suitable one in the determination of the eigenvalue and the eigenfunction of the problem.
As the functions $h(r)$ and $h_n(r)$ are equal, we use Eq. (5) and Eq. (9) to obtain the energy equation as

$$Ar + B \pm (2\alpha_2 r + \alpha_1) = C_n - n\left[\pm (2\alpha_2 r + \alpha_1) \right], \tag{43}$$

where C_n is an integration constant which couples with the parameters of potential. Eq. (43) leads us to have two distinct choices $++$ and $--$, which are given by **I** and **II** as follows

$$\mathbf{I}: \begin{cases} 2\alpha_2 + A = -2n\alpha_2 \\ B + \alpha_1 = C_n - n\alpha_1 \end{cases} \qquad \mathbf{II}: \begin{cases} -2\alpha_2 + A = 2n\alpha_2 \\ B - \alpha_1 = C_n + n\alpha_1 \end{cases}.$$ (44)

The choice of $--$ and set **II** results on the relation $A + 2(n+1)\alpha_2 = 0$ from which we can write:

$$\frac{4\xi_4\xi_2 + [\xi_3]^2 - 4\xi_4\sqrt{\xi_4}\sqrt{\xi_0+1}}{4\xi_4} = 2(n+1)\sqrt{\xi_4}.$$ (45)

Using Eq. (35) and Eq. (45), we obtain the expression below:

$$E_{nlm} = d - \frac{a^2}{4b} + 2\sqrt{\frac{2b}{M}}\left(2(n+1) + 2\sqrt{2Mg + \left[l - \left(1 - \frac{1}{\alpha}\right)m\right]\left[l - \left(1 - \frac{1}{\alpha}\right)m+1\right] + \frac{1}{4}} \right).$$ (46)

We note that the presence of the cosmic string parameter α breaks the degeneracy in all the states with $l \neq 0$. When $\alpha \to 1$ and $d \to 0$, we recover the results obtained in [26, 33]. Moreover, for $\alpha \to 1$, $d \to 0$, $a = 0$ and $g = 0$ we obtain the energy spectrum of a spherical quantum harmonic oscillator [26].

For the wave function, it is easy to obtain $\phi(r)$ from Eq. (4) as

$$\phi(r) = r^{\left(\alpha_0 + \frac{1}{2}\right)} e^{\left(\alpha_1 r + \frac{1}{2}\alpha_2 r^2\right)},$$ (47)

and $\rho(r)$ from Eq. (7) as

$$\rho(r) = r^{2\alpha_0} e^{2\left(\alpha_1 r + \frac{1}{2}\alpha_2 r^2\right)}.$$ (48)

Then we use Eq. (6) to obtain the function $Y_n(r)$ as

$$Y_n(r) = B_n r^{-2\alpha_0} e^{-2\left(\alpha_1 r + \frac{1}{2}\alpha_2 r^2\right)} \frac{d^n}{dr^n}\left[r^{n+2\alpha_0} e^{2\left(\alpha_1 r + \frac{1}{2}\alpha_2 r^2\right)} \right].$$ (49)

From Eq. (2) the radial eigenfunctions are then

$$\psi_{nl}(r) = N_{nl} r^{-\alpha_0 + \frac{1}{2}} e^{-\left(\alpha_1 r + \frac{1}{2}\alpha_2 r^2\right)} \frac{d^n}{dr^n}\left[r^{n+2\alpha_0} e^{2\left(\alpha_1 r + \frac{1}{2}\alpha_2 r^2\right)} \right],$$ (50)

where N_{nl} is the normalization factor, and $\alpha_0, \alpha_1, \alpha_2$ are given from set **II**

4. THERMODYNAMIC PROPERTIES OF THE $q\bar{q}$ SYSTEM

To consider the thermodynamic properties of heavy quarkonia within cosmic-string framework, the starting point is the partition function [34, 35]. From a statistical mechanical point of view, the partition function can be constructed as follow:

$$\begin{aligned} Z(\beta) &= \sum_{n=0}^{\infty} e^{-\beta E_n} \\ &= e^{-\beta\left[-\frac{a^2}{4b} + 4\sqrt{\frac{2b}{\mu}}\left(1 + \sqrt{2\mu g + \left[l-\left(1-\frac{1}{\alpha}\right)m\right]\left[l-\left(1-\frac{1}{\alpha}\right)m+1\right]+\frac{1}{4}}\right)\right]} \sum_{n=0}^{\infty} e^{-4\beta\sqrt{\frac{2b}{\mu}}n}, \\ &= \frac{1}{2} e^{-\beta\left[2\sqrt{\frac{2b}{\mu}} + \left[-\frac{a^2}{4b} + 4\sqrt{\frac{2b}{\mu}}\left(1 + \sqrt{2\mu g + \left[l-\left(1-\frac{1}{\alpha}\right)m\right]\left[l-\left(1-\frac{1}{\alpha}\right)m+1\right]+\frac{1}{4}}\right)\right]\right]} \mathrm{csch}\left(2\beta\sqrt{\frac{2b}{\mu}}\right) \end{aligned}$$ (51)

here $\beta = k_B T$, where k_B is the Boltzmann constant and T is the absolute temperature of the system. Once the partition function is obtained, we can have the Helmholtz free energy as:

$$F = -\frac{1}{\beta}\ln Z(\beta)$$

$$= \left[-\frac{a^2}{4b} + 4\sqrt{\frac{2b}{\mu}}\left(1 + \sqrt{2\mu g + \left[l - \left(1 - \frac{1}{\alpha}\right)m\right]\left[l - \left(1 - \frac{1}{\alpha}\right)m + 1\right] + \frac{1}{4}}\right)\right] + \frac{1}{\beta}\ln\left(1 - e^{-4\beta\sqrt{\frac{2b}{\mu}}}\right)$$

$$= \left[-\frac{a^2}{4b} + 4\sqrt{\frac{2b}{\mu}}\left(1 + \sqrt{2\mu g + \left[l - \left(1 - \frac{1}{\alpha}\right)m\right]\left[l - \left(1 - \frac{1}{\alpha}\right)m + 1\right] + \frac{1}{4}}\right)\right] - 2\sqrt{\frac{2b}{\mu}}$$

$$+ \frac{1}{\beta}\ln\left(2\sinh\left(2\beta\sqrt{\frac{2b}{\mu}}\right)\right)$$

(52)

From the Helmholtz free energy, we can obtain the other statistical quantities in a straightforward manner. The entropy of the system can be obtained as

$$S = -k_B\beta^2\frac{\partial F}{\partial \beta}$$

$$= -\ln\left[1 - e^{-4\beta\sqrt{\frac{2b}{\mu}}}\right] + 4\beta\sqrt{\frac{2b}{\mu}}\frac{e^{-4\beta\sqrt{\frac{2b}{\mu}}}}{\left(1 - e^{-4\beta\sqrt{\frac{2b}{\mu}}}\right)}$$

(53)

$$= -\ln\left[2e^{-2\beta\sqrt{\frac{2b}{\mu}}}\sinh\left(2\beta\sqrt{\frac{2b}{\mu}}\right)\right] + 2\beta\sqrt{\frac{2b}{\mu}}e^{-2\beta\sqrt{\frac{2b}{\mu}}}\operatorname{csch}\left(2\beta\sqrt{\frac{2b}{\mu}}\right)$$

The internal energy U is defined as:

$$U = -\frac{\partial}{\partial\beta}(\beta F) = -\frac{\partial\ln Z(\beta)}{\partial\beta}$$

$$= \left[-\frac{a^2}{4b} + \sqrt{\frac{2b}{\mu}}\left(1 + \sqrt{2\mu g + \left[l - \left(1 - \frac{1}{\alpha}\right)m\right]\left[l - \left(1 - \frac{1}{\alpha}\right)m + 1\right] + \frac{1}{4}}\right)\right] + \frac{4\sqrt{\frac{2b}{\mu}}e^{-4\beta\sqrt{\frac{2b}{\mu}}}}{\left(1 - e^{-4\beta\sqrt{\frac{2b}{\mu}}}\right)}$$

(54)

$$= \left[-\frac{a^2}{4b} + 4\sqrt{\frac{2b}{\mu}}\left(1 + \sqrt{2\mu g + \left[l - \left(1 - \frac{1}{\alpha}\right)m\right]\left[l - \left(1 - \frac{1}{\alpha}\right)m + 1\right] + \frac{1}{4}}\right)\right] + \sqrt{\frac{2b}{\mu}}e^{-2\beta\sqrt{\frac{2b}{\mu}}}\operatorname{csch}\left(2\beta\sqrt{\frac{2b}{\mu}}\right)$$

Then from the internal energy we can compute the specific heat capacity at constant volume C_v as

$$C_v = -\beta^2\frac{\partial U}{\partial\beta}$$

$$= 16k_B\beta^2\sqrt{\frac{2b}{\mu}}\frac{e^{-4\beta\sqrt{\frac{2b}{\mu}}}\left[1 + \left(\sqrt{\frac{2b}{\mu}} - 1\right)e^{-4\beta\sqrt{\frac{2b}{\mu}}}\right]}{\left(1 - e^{-4\beta\sqrt{\frac{2b}{\mu}}}\right)^2}$$

(55)

$$= 4k_B\beta^2\sqrt{\frac{2b}{\mu}}\left[1 + \left(\sqrt{\frac{2b}{\mu}} - 1\right)e^{-4\beta\sqrt{\frac{2b}{\mu}}}\right]\operatorname{csch}^2\left(2\beta\sqrt{\frac{2b}{\mu}}\right)$$

5. RESULTS AND DISCUSSION

In this section, we discuss the effect of cosmic-string geometry on thermodynamic properties and spectrum of heavy quarkonia. Fig. 1,2 and 3 show the plots of the radial wave functions of $c\bar{c}$ mesons for the $1P$, $2P$ and $3P$ states

respectively, at different values of the parameter of the topology. Whereas, in Fig. 4,5 and 6, variations of the radial wave functions of $b\bar{b}$ mesons are plotted for the $1P$, $2P$ and $3P$ states respectively, at different values of the parameter α.
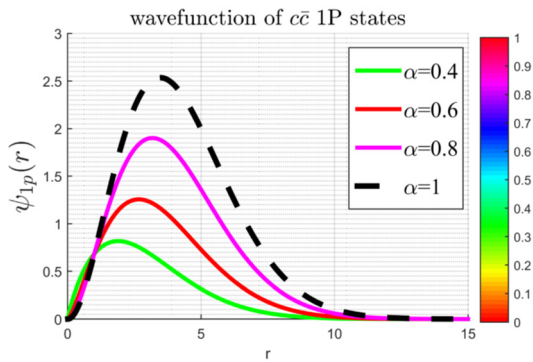

Figure 1. Ground states wave functions of $c\bar{c}$ meson plotted against of the radius r at different values of α with $l=1$, $m_l = +1$
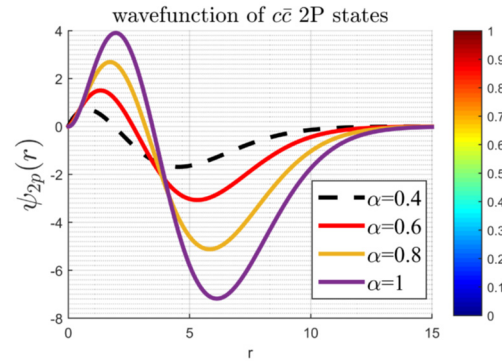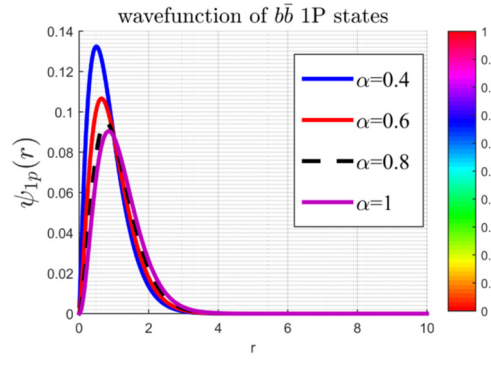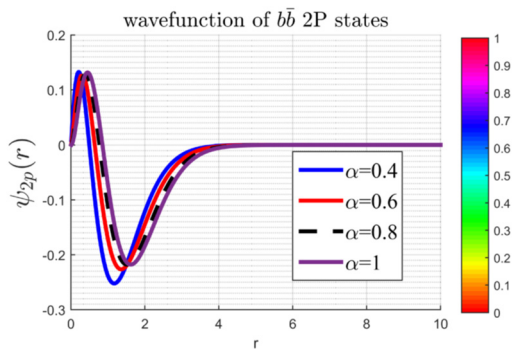

Figure 2. Radial wave functions of first excited states of $c\bar{c}$ meson plotted against of the radius r at different values of α with $l=1$, $m_l = +1$
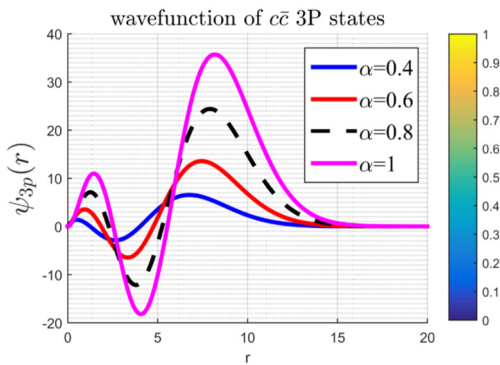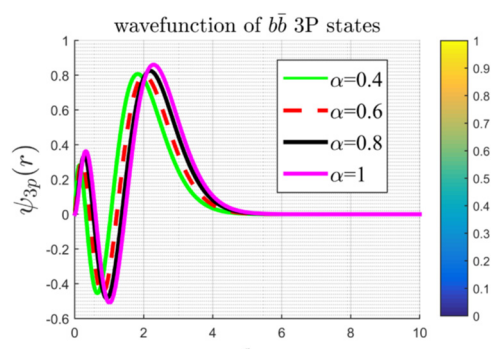

Figure 3. Radial wave functions of second excited states of $c\bar{c}$ meson plotted against of the radius r at different values of α with $l=1$, $m_l = +1$

Figure 4. Ground states wave functions of $b\bar{b}$ meson plotted against of the radius r at different values of α with $l=1$, $m_l = +1$

Figure 5. Radial wave functions of first excited states of $b\bar{b}$ mesons plotted against of the radius r at different values of α with $l=1$, $m_l = +1$

Figure 6. Radial wave functions of second excited states of $b\bar{b}$ mesons plotted against of the radius r at different values of α with $l=1$, $m_l = +1$

It appears that the peaks of the wave functions are shifted backward for small values of α, and its values shift to higher values by increasing α for $c\bar{c}$, and by decreasing α for $b\bar{b}$. In Fig. 7,8 and 9 are plotted the radial functions of probability densities of $c\bar{c}$ mesons for the $1P$, $2P$ and $3P$ states respectively, considering different values of the topological parameter α. Whereas, in Fig. 10,11 and 12 are plotted the radial functions of probability densities of $b\bar{b}$ mesons for the $1P$, $2P$ and $3P$ states respectively It is observed that the behavior is the same for any P – state, but with some shift in the peaks toward the origin. Considering $c\bar{c}$ and $b\bar{b}$ mesons, the peaks are shifted toward the origin as α decrease.
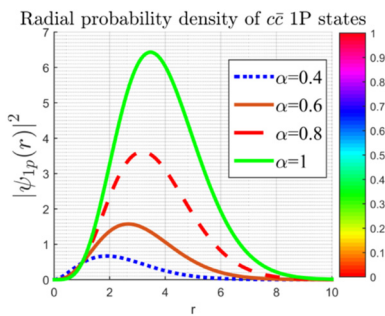
Figure 7. Density functions of radial probability for ground states of $c\bar{c}$ meson plotted against of the radius r at different values of α with l=1, $m_l = +1$
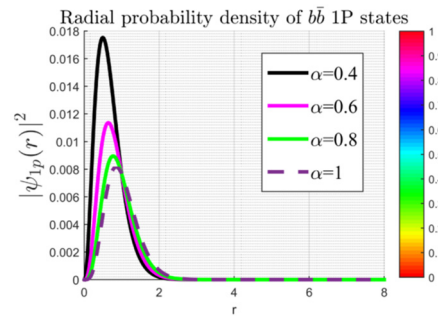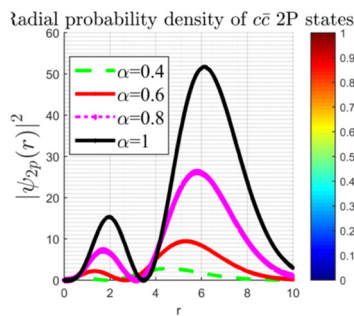

Figure 8. Density functions of radial probability for ground states of $b\bar{b}$ mesons plotted against of the radius r at different values of α with l=1, $m_l = +1$

Figure 9. Density functions of radial probability for first excited states of $c\bar{c}$ meson plotted against of the radius r at different values of α with l=1, $m_l = +1$
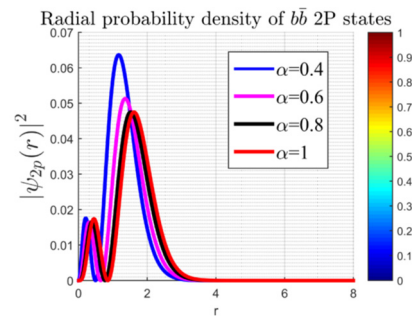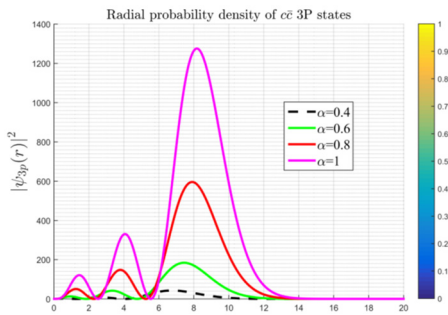

Figure 10. Density functions of radial probability for first excited states of $b\bar{b}$ meson plotted against of the radius r at different values of α with l=1, $m_l = +1$

Figure 11. Density functions of radial probability for second excited states of $c\bar{c}$ meson plotted against of the radius r at different values of α with l=1, $m_l = +1$
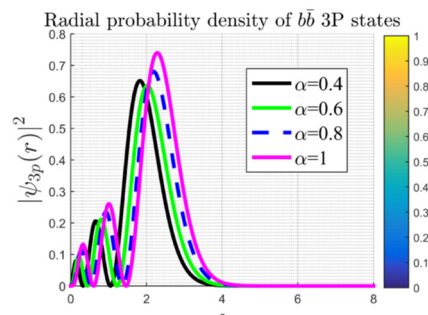

Figure 12. Density functions of radial probability for second excited states of $b\bar{b}$ meson plotted against of the radius r at different values of α with l=1, $m_l = +1$

To calculate the thermodynamic properties of quark-antiquark systems, we have employed tools from statistical mechanics, taking as a starting point the canonical partition function of the system, from which the other statistical quantities were calculated in a straightforward manner. Next, we depict the statistical properties of $c\bar{c}$ and $b\bar{b}$ mesons in Figs. 13-22. In our model, the effect of the cosmic-string appears only when $l \neq 0$. Indeed, from Eq. (51) we clearly see that $S-$ states are not influenced by the cosmic-string geometry but by the usual Minkowski geometry because when $l = 0$ we equally have $l_{(\alpha)} = 0$, and all the quantities become α – independent. In fact, setting the cosmic-string parameter to 1 automatically eliminate the effect of topological defect. For this reason, much emphasis were placed on the study of states with $l \neq 0$, namely the $P-$ states.

In Fig. 13,14, we have plotted the canonical partition function respectively for $c\bar{c}$ and $b\bar{b}$ quarkonia in terms of β for different values of the cosmic-string parameter α. It is clearly seen that by decreasing the value of α, all the curves are separated from the classical Minkowski curve ($\alpha = 1$). For all the values of the topological parameter the behavior is the same but with different magnitudes. Moreover, the splitting increases as α decreases and then the partition function decreases with increasing β which is in agreement with [36, 37]. In [36], the author applied the deformed five parameter exponential potential and observed that with increasing β, the canonical partition function for the Minkowskian case decreases monotonically.
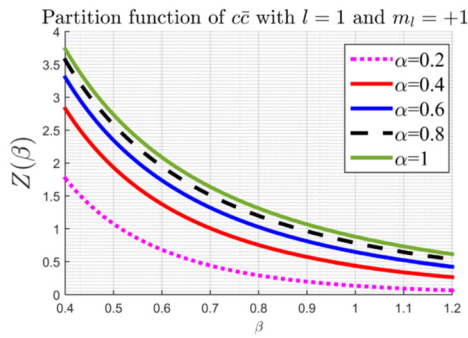
Figure 13. Density functions of radial probability for second excited states of $c\bar{c}$ meson plotted against of the radius r at different values of α with $l=1$, $m_l = +1$
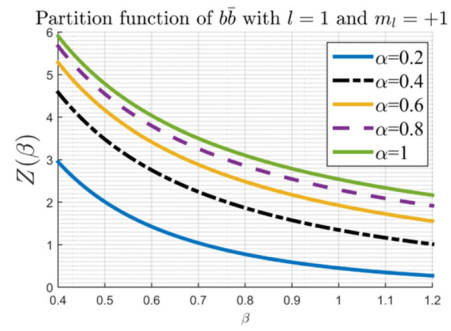

Figure 14. Density functions of radial probability for second excited states of $b\bar{b}$ meson plotted against of the radius r at different values of α with $l=1$, $m_l = +1$

In Fig. 15,16 The Helmholtz free energy is plotted as a function of β respectively for $c\bar{c}$ and $b\bar{b}$ mesons.

Figure 15. Density functions of radial probability for second excited states of $c\bar{c}$ meson plotted against of the radius r at different values of α with $l=1$, $m_l = +1$
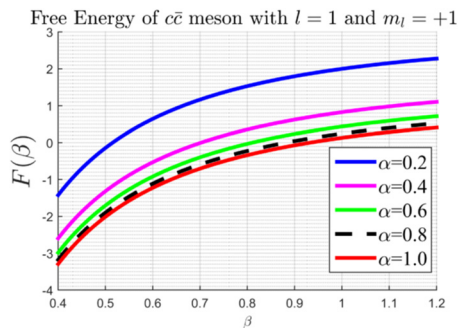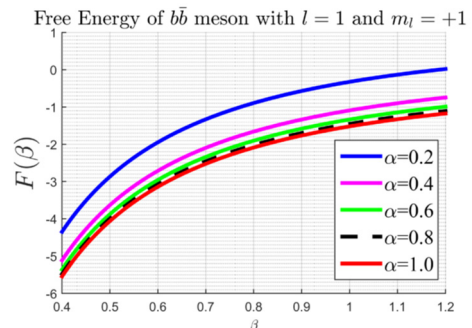

Figure 16. Density functions of radial probability for second excited states of $b\bar{b}$ meson plotted against of the radius r at different values of α with $l=1$, $m_l = +1$

The effect of the cosmic-string geometry clearly appears when α takes values different from $\alpha = 1$ (classical Minkowski space-time). It is found that the Helmholtz function increases monotonically with increasing β, and the curves with $\alpha \neq 1$ are separated from the classical Minkowski curve. Moreover, the splitting is important for small values of α. In [34], the author treated quark-gluon plasma as composed of light quarks only, which interact weakly. They observed that the Helmholtz free energy decreases as the temperature increases. In [35], Modarres and Gholizade calculated the Helmholtz function of a neutral particle and observed that the free energy of the system decreases as the temperature increases. In the present model, the behavior of charm and bottom quark matter is in agreement with [34, 35, 38].

In Fig. 17,18 the internal energy is plotted against β for different values of α, respectively for $c\bar{c}$ and $b\bar{b}$ mesons. It reveals that, $U(\beta)$ decreases with increasing β, and its values shift to lower values by increasing the parameter of the topology α.

Figure 17. Density functions of radial probability for second excited states of $c\bar{c}$ meson plotted against of the radius r at different values of α with $l=1$, $m_l = +1$
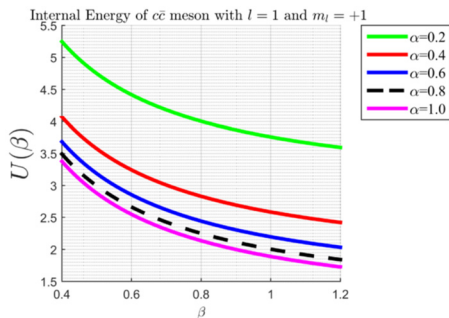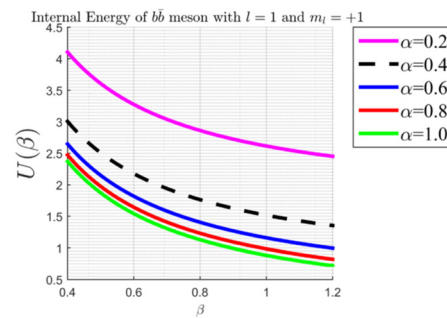

Figure 18. Density functions of radial probability for second excited states of $b\bar{b}$ meson plotted against of the radius r at different values of α with $l=1$, $m_l = +1$

In [38], the authors studied thermodynamic properties of neutral particles in a cosmic-string background from non-relativistic Schrödinger-Pauli equation. They observed that the internal energy of the system increases as the temperature increases. Thus, the conclusion of the present work for internal energy is the same with recent works [36, 37, 38].

The entropy $S(\beta)$ and the specific heat capacity $C_v(\beta)$ are plotted against β respectively in Fig. 19 and Fig. 21 $c\bar{c}$ meson and in Fig. 20 and Fig. 22 $b\bar{b}$ meson. These figures show that the entropy and the specific heat capacity of $c\bar{c}$ and $b\bar{b}$ mesons are not influenced by the parameters of topology, and are similar to the solution for a at Minkowski space-time. In [38] a similar result was obtained for neutral particles, showing the non-dependence on topological defect of heat capacity and entropy, which is in total agreement with the present work.
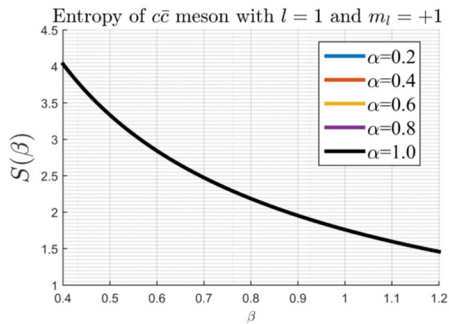

Figure 19. Density functions of radial probability for second excited states of $c\bar{c}$ meson plotted against of the radius r at different values of α with $l=1$, $m_l = +1$

Figure 20. Density functions of radial probability for second excited states of $b\bar{b}$ meson plotted against of the radius r at different values of α with $l=1$, $m_l = +1$

Figure 21. Density functions of radial probability for second excited states of $c\bar{c}$ meson plotted against of the radius r at different values of α with $l=1$, $m_l = +1$
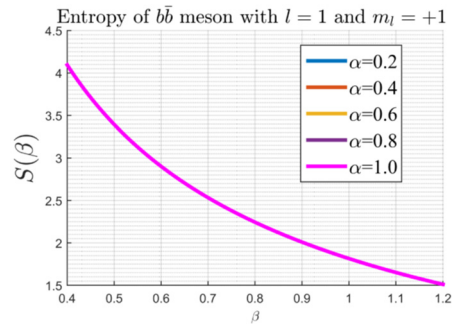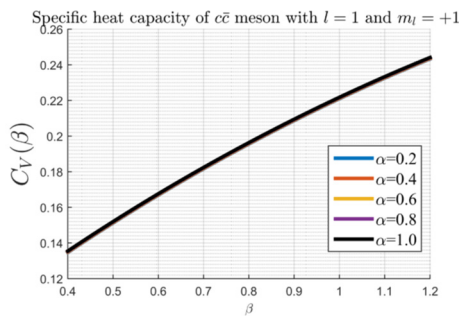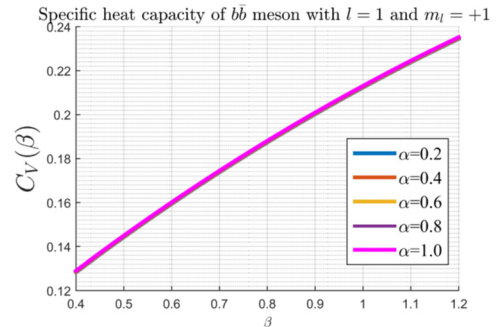

Figure 22. Density functions of radial probability for second excited states of $b\bar{b}$ meson plotted against of the radius r at different values of α with $l=1$, $m_l = +1$

6. CONCLUSION

In this work, we have investigated the effects of the gravitational field of a topological defect on thermodynamical properties of heavy quarkonia. We have used the extended Nikiforov-Uvarov method to solve the radial Schrödinger wave equation in the space-time of a cosmic string, for the potential $V(r) = -\dfrac{K}{r} + \alpha r + \dfrac{g}{r^2} + br^2$. We obtain the radial wave functions of $c\bar{c}$ and $b\bar{b}$ mesons as well as the energy eigenvalues, which are shifted from the usual Minkowski energies. From this, we have considered all the statistical quantities using the canonical partition function of the system. The wave functions and the thermodynamic properties were analyzed graphically. It was observed that the peaks of radial functions of probability densities are shifted toward the origin as α decrease. The thermodynamic quantities present a shift compared to the classic limit; this difference becomes more important for small values of the cosmic-string parameter. The partition function shifts to lower values as α decrease, the Helmholtz function increases monotonically with increasing β, and the curves with $\alpha \neq 1$ are separated from the Minkowski curve, then the values of the internal energy are shifted to lower values by increasing the parameter of the topology. Meanwhile the specific heat capacity and the entropy are not influenced by the topological defect.

Declaration of competing interest. The authors declare that they have no known competing financial interests or personal relationships that could have appeared to influence the work reported in this paper.

ORCID IDs

André Aimé Atangana Likéné, https://orcid.org/0000-0003-2642-7400
Jean Marie Ema'a Ema'a, https://orcid.org/0000-0002-6162-7961
Germain Hubert Ben-Bolie, https://orcid.org/0000-0002-0564-4548

REFERENCES

[1]   L.R. Ribeiro et al, Phys. Lett. A, **348**, 135 (2006). https://doi.org/10.1016/j.physleta.2005.08.046
[2]   K. Bakke, Int. J. Mod. Phys. A, **26**, 4239 (2011). https://doi.org/10.1142/S0217751X11054437
[3]   Y. Aharonov, and D. Bohm, Phys. Rev. **115**, 485 (1959). https://doi.org/10.1103/PhysRev.115.485
[4]   K.W.B. Kibble, J. Phys. A: Math. Gen. **9**(8), 1387 (1976). https://doi.org/10.1088/0305-4470/9/8/029
[5]   K.W.B. Kibble, Phys. Rev. D, **26**(2), 435 (1982). https://doi.org/10.1103/PhysRevD.26.435
[6]   A. Vilenkin, and E.P.S. Shellard, *Cosmic Strings and Other Topological Defects*, (Cambridge University Press, Cambridge, U.K., 1994).
[7]   J. Rocher, Thèse de Doctorat, Contraintes cosmologiques sur la physique de l'univers primordial, Universit de Paris XI-Orsay, 2005.
[8]   L. Bergström, and A. Goobar, *Cosmology and Particle Astrophysics*, 2nd edition (Springer, 2006).
[9]   A.-C. Davis, and T.W. Kibble, Contemp. Phys. **46**, 313 (2005). https://doi.org/10.1080/00107510500165204
[10] N.G. Marchuk, Nuovo. Cimento. B, **115**, 11 (2000). https://doi.org/10.48550/arXiv.math-ph/0010045
[11] C. Furtado, V.B. Bezerrae, and F. Moraes, Phys. Lett. A, **289**, 160 (2001). https://doi.org/10.1016/S0375-9601(01)00615-6
[12] C. Furtado, B.G.C. da Cunha, F. Moraes, E.R.B. Mello, and V.B. Bezzerra, Phys. Lett. A, **195**, 90 (1994), https://doi.org/10.1016/0375-9601(94)90432-4
[13] J. Audretsch, and A. Economou, Phys. Rev. D, **44**, 3774 (1991). https://doi.org/10.1103/PhysRevD.44.3774
[14] D.D. Harari, and V.D. Skarzhinsky, Phys. Lett. B, **240**, 322 (1990). https://doi.org/10.1016/0370-2693(90)91106-L
[15] J.R. Gott III, Astrophys. **288**, 422 (1985). https://adsabs.harvard.edu/pdf/1985ApJ...288..422G
[16] V.B. Bezerra, Phys. Rev. D, **35**, 2031 (1987). https://doi.org/10.1103/PhysRevD.35.2031
[17] W. Florkowski, *Phenomenology of Ultra-Relativistic Heavy-Ion Collisions*, (World Scientific Singapore, 2010), pp. 416.
[18] U. Kalade, and B.K. Patra, Phys. Rev. C, **92**, 024901 (2015). https://doi.org/10.1103/PhysRevC.92.024901
[19] T. Matsui, and H. Satz, Phys. Lett. B, **178**, 416 (1986). https://doi.org/10.1016/0370-2693(86)91404-8
[20] R.C. Hwa, and X.N. Wang, editors, *Quark-Gluon Plasma* 3, (World Scientific Publishing, 2004), pp. 788.
[21] V.S. Filinov, M. Bonitz, Y.B. Ivanov, M. Ilgenfritz, and V.E. Fortov, Contrib. Plasma Phys. **55**, 203 (2015). https://doi.org/10.1002/ctpp.201400056
[22] M. Schleif, and R. Wunsch, Eur. Phys. J. A, **1**, 171 (1998). https://doi.org/10.1007/s100500050046
[23] M. Abu-Shady, Inter. J. Theor. Phys. **52**, 1165 (2013). https://doi.org/10.1007/s10773-012-1432-z
[24] M. Abu-Shady, Inter. J. Theor. Phys. **54**, 1530 (2015). https://doi.org/10.1007/s10773-014-2352-x
[25] D. Nga Ongodo, J.M. Ema'a Ema'a, P. Ele Abiama, and G.H. Ben-Bolie, Int. J. Mod. Phys. E, **28**, 1950106 (2019). https://doi.org/10.1142/S0218301319501064
[26] Al-Jamel, Mod. Phys. Lett. A, **33**, 1850185 (2018). https://doi.org/10.1142/S0217732318501857
[27] H. Karayer, D. Demirhan, and F. Büyükilic, J. Math. Phys. **59**, 053501 (2008). https://doi.org/10.1063/1.5022008
[28] M.D. Katanaev, and I.V. Volovich, "Theory of defects in solids and three-dimensional gravity", Annals of Physics, **216**(1), 1 1992. https://doi.org/10.1016/0003-4916(52)90040-7
[29] C. Furtado, and F. Moraes, Phys. Lett. A, **188**(4-6), 394 (1994). https://doi.org/10.1016/0375-9601(94)90482-0
[30] C.R. Muniz, V.B. Bezerra and M.S. Cunha, Ann. Phys. **350**, 105 (2014). https://doi.org/10.1016/j.aop.2014.07.017
[31] V.F. Mukanov, H.A. Feldman, and R.H. Brandenberger, Physical Report **215**, 203 (1992). https://doi.org/10.1016/0370-1573(92)90044-Z
[32] J.L. Domenech-Garret, and M.A. Sanchis-Lozano, Physics Letters B, 669(1), 52 (2008). https://doi.org/10.1016/j.physletb.2008.09.021
[33] Y. Cançelik, and B. Gönül, Mod. Phys. Lett. A, **29**, 1450170 (2014). https://doi.org/10.1142/S0217732314501703
[34] M. Modarres, and A. Mohamadnejad, Phys. Part. Nucl. Lett. **10**, 99 (2013). https://doi.org/10.1134/S1547477113020106
[35] M. Modarres, and H. Gholizade, Int. J. Mod. Phys. E, **17**, 1335 (2008). https://doi.org/10.1142/S0218301308010453
[36] A.N. Ikot, B.C. Lutfuoglu, M.I. Ngweke, M.E. Udoh, S. Zare, and H. Hassanabadi, Eur. Phys. J. Plus, **131**, 419 (2016). https://doi.org/10.1140/epjp/i2016-16419-5
[37] W.A. Yahua, and K.J. Oyewumi, J. Asso. Arab. Univ. Bas. App. Scie, **21**, 53 (2016). https://doi.org/10.1016/j.jaubas.2015.04.001
[38] H. Hassanabadi, and M. Hosseinpoura, Eur. Phys. J. C, **76**, 553 (2016). https://doi.org/10.1140/epjc/s10052-016-4392-2

**ВПЛИВ ГРАВІТАЦІЙНОГО ПОЛЯ НА ТОПОЛОГІЧНИЙ ДЕФЕКТ
НА СТАТИСТИЧНІ ВЛАСТИВОСТІ ВАЖКИХ КВАРК-АНТИКВАРКОВИХ СИСТЕМ**
**Андре Аме Атангана Лікене[а,с], Алі Зарма[а], Дьєдонне Нга Онгодо[а],
Жан Марі Ема'а Ема'а[b], Патріс Еле Абіам[а,с], Жермен Юбер Бен-Болі[а]**
*[а]Лабораторія атомної, молекулярної та ядерної фізики, кафедра фізики, природничий факультет
Університет Яунде І, P.O. Box 812, Яунде, Камерун*
[b]Нгаундере Вище педагогічне училище, факультет фізики, Університет Маруа, P.O. Box 55, Бертуа, Камерун
[с]Секція ядерних технологій (NTS), Інститут геологічних і гірничих досліджень, P.O. Box 4110, Яунде, Камерун

У цій статті ми визначаємо власні енергії, власні функції та статистичні властивості нерелятівістського важкого кварконію, що взаємодіє з розширеним потенціалом Корнеля в просторі-часі, створеному космічною струною. Ми розширюємо потенціал Корнеля, додаючи обернений квадратний потенціал плюс квадратичний потенціал. Ми розрахували власні значення енергії та відповідні власні стани за допомогою розширеного методу Нікіфорова-Уварова (ENU). Потім на основі рівняння енергетичних спектрів обчислюються термодинамічні властивості, такі як статистична сума, ентропія, вільна енергія, середня енергія та питома теплоємність у просторі-часі космічної струни. На наступному кроці ми досліджуємо вплив параметра космічної струни на квантові стани важких кварконіїв та їх статистичні властивості.

Ключові слова: термодинамічні властивості, кварк, хвильове рівняння Шредінгера, топологічний дефект, простір-час, космічна струна, розширений потенціал Корнела, мезон, розширений метод Нікіфорова-Уварова.

MOLECULAR DOCKING OF MONOMETHINE CYANINE DYES TO LYSOZYME AMYLOID FIBRILS[†]

Olga Zhytniakivska[a,*], Uliana Tarabara[a], Atanas Kurutos[b,c], Kateryna Vus[a],
Valeriya Trusova[a], Galyna Gorbenko[a]

aDepartment of Medical Physics and Biomedical Nanotechnologies, V.N. Karazin Kharkiv National University
4 Svobody Sq., Kharkiv, 61022, Ukraine
bInstitute of Organic Chemistry with Centre of Phytochemistry, Bulgarian Academy of Sciences
Acad. G. Bonchev str., bl. 9, 1113, Sofia, Bulgaria
cDepartment of Pharmaceutical and Applied Organic Chemistry, Faculty of Chemistry and Pharmacy
Sofia University St. Kliment Ohridski, 1 blv. J. Bourchier, Sofia, 1164, Bulgaria
*Corresponding Author: olga.zhytniakivska@karazin.ua

Protein aggregation into highly ordered supramolecular aggregates (amyloid fibrils) is the hallmark of many human diseases including the neurological disorders (Parkinson's, Alzheimer's and Huntington's diseases), type II diabetes, systemic amyloidosis, spongiform encephalopathies, etc. One of the simplest and effective methods for the identification and characterization of amyloid fibrils *in vitro* and the visualization of amyloid inclusions *in vivo* is based on the use of optical probes sensitive to the beta-pleated motifs. To design the new amyloid-sensing dyes or to optimize the use of the existing amyloid markers, it is crucial to have the sufficient knowledge of the fibril-dye binding interactions at the molecular and atomic levels. One of the most powerful tools capable of providing the atomic-level insights into the mechanisms of various types of biomolecular interactions is the molecular docking technique. In the present study, the molecular docking has been employed to investigate the interactions between the monomethine cyanine dyes and the lysozyme amyloid fibrils constructed from the K-peptide of lysozyme, GILQINSRW (the residues 54–62 of the wild-type protein). Using the AutoDOCK and the protein-ligand interaction profiler PLIP it was found that: i) the monomethines interact with the fibril surface (with the aromatic residues on the top of β-sheet or with the edges of the β-sheet); ii) the dye-fibril binding is governed by hydrophobic interactions, salt bridges and hydrogen bonds between the aliphatic substituents on the nitrogen atom of benzothiazole part of the dye molecules and amino acid side chains; iii) the variations in the cyanine structure and the lysozyme amyloid twisting do not exert significant effect on the binding mode of cyanines.

Keywords: Monomethine cyanine dyes, lysozyme amyloid fibrils, molecular docking.
PACS: 87.14.C++c, 87.16.Dg

In the recent two decades the molecular docking technique have continuously attracted tremendous interest as a successful structure-based in silico method to gain atomic-level insights into the mechanisms of various types of biomolecular interactions [1-3], high-throughput drug screening [4-6] or understanding structure-activity relationships without knowing a priori the chemical structure of target modulators [7,8]. More specifically, the molecular docking has been used i) to develop antiviral drugs against the SARS-CoV-2 [9,10], inhibitors of hepatitis B [11] and HIV viruses [12]; ii) to determine a potential anticancer chemotherapeutic agents [13,14]; iii) for enzyme engineering [15]; iv) to assess the antithrombotic activity of the peptides [16]; v) to characterize the ligand-macromolecule of macromolecule-macromolecule interactions [17,18]; vi) to evaluate the ligand-receptor binding affinity [19, 20], to name only a few. In the above studies the molecular docking approach was used to pursue two basic goals: i) prediction of the ligand conformation along with its position and orientation within binding sites and ii) evaluation of the binding affinity [1]. One area where molecular docking appeared to be especially useful concerns the atomic-level characterization of the interactions between ligands and proteins in the amyloid state [21-24]. In this context, the detailed knowledge of the molecular interactions involved in the ligand-protein complexation made it possible to design the inhibitor compounds against amyloid aggregation [21,22] and to develop and improve the specific markers for spectroscopic detection of amyloid fibrils [23,24]. Notably, despite significant progress in the synthesis and characterization of the optical probes for detection of protein aggregates, the highly effective amyloid markers are still needed. Among the compounds possessing the excellent amyloid-sensing potential are cyanine dyes [25-33]. More specifically, cyanines have been applied: i) for detection of amyloid fibrils *in vitro* [25-27], ii) for *in vivo* fluorescent imaging of Aβ plaques in the Alzheimer's disease brain [28,29]; for monitoring the fibrillization kinetics of amyloid paired helical filaments [30]; for preventing and modulating protein fibrillization [31-33], to name only a few. Despite the numerous applications of the cyanine dyes in the amyloid research, the structural requirements for an ideal amyloid tracer remain unclear. Besides, the substituents in heterocyclic residues as well as the N-alkyl chain length have been found to modulate the amyloid-sensing ability of cyanine dyes [25,31].

In the present work the molecular docking approach was used to investigate the atomistic details of the interactions between the novel monomethine cyanine dyes (Figure 1) and the model amyloid fibrils of lysozyme. The aim of the study was to determine both the potential binding sites of the cyanine dyes in the fibrillar lysozyme and to uncover the impact of the cyanine structure on the molecular interactions involved in the dye-protein complexation.
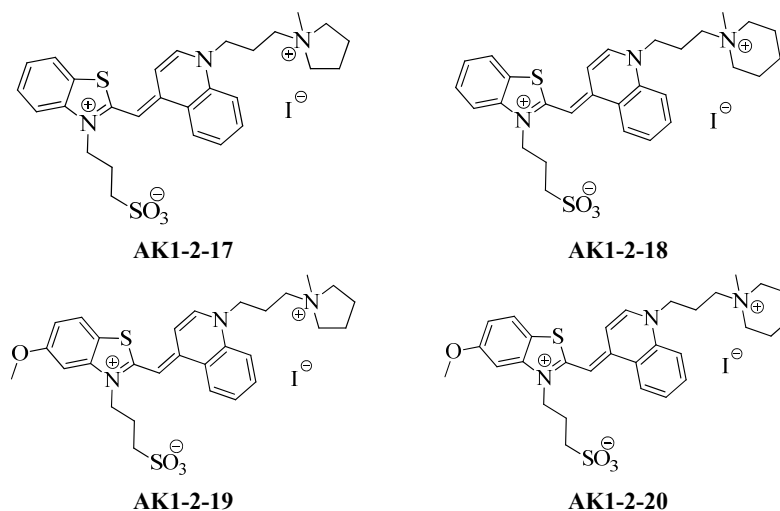

Figure 1. Structural formulas of monomethine cyanine dyes

METHODS

The model fibrils were built from the K-peptide of lysozyme, GILQINSRW (the residues 54–62 of the wild-type protein), using the CreateFibril tool as described previously [34]. More specifically, the lysozyme dimer was initially generated from the K-peptide monomer in the β-strand conformation using the PatchDock and Firedock tools [35,36]. Then, the CreateFibril software was used to generate the identical copies of the lysozyme dimer through stacking them side-by-side [37]. In such a manner, the lysozyme model fibrils with the length of 10 protein monomers were constructed. The distance between β-strands along the fibril axis and protofilament separation perpendicular to fibril axis were set as 5 Å. While creating the lysozyme fibrillar structures, we varied the rotation angle of monomers along the fibril axis from 0 to 20° degrees. In such a manner, five lysozyme fibrillar structures were created with the twisting angle 0°, 5°, 10°, 15° and 20°, referred to here as LzF-0, LzF-5, LzF-10, LzF-15, and LzF-20, respectively.

To define the most energetically favorable binding sites for the examined monomethine cyanine dyes on the firbrillar lysozyme, the molecular docking studies were performed using the AutoDock (version 4.2) incorporated in the PyRx software (version 0.8) [38]. AutoDock belongs to the non-commercial docking programs that implement a stochastic Lamarckian genetic algorithm for computing ligand conformations [38]. The thermodynamic stability of the ligand-receptor complexes was achieved by minimization of the scoring function which is based on the AMBER force field including van der Waals, hydrogen bonding, electrostatic interactions, conformational entropy and desolvation terms [38]. The AutoDock approach assumes the flexible ligand while the receptor is kept rigid during the docking procedure. The dye structures were built in MarvinSketch (version 18.10.0) and optimized in Avogadro (version 1.1.0) [39,40]. The docking poses were visualized with the UCSF Chimera software (version 1.14) [41]. To characterize the nature of the dye-protein interactions the protein-ligand interaction profiler PLIP (https://plip-tool.biotec.tu-dresden.de/plip-web/plip/index) was used [42].

RESULTS AND DISCUSSION

Amyloid fibrils, the cross-β-sheet structures with β-strands orienting perpendicularly to the fibril long axis and β-sheets propagating in its direction, are known to provide several binding sites for small molecules (drugs, dyes, etc) [43,44]. These binding sites are located in the channels formed by the amino acid side chains of β-strands; exposed grooves on the β-sheet surface and the ends of the extended β-sheet [43,44]. At the first step of the study, to identify the monomethine-protein binding sites, as well as the nature of interactions involved in the dye complexation with the lysozyme fibrils, the AutoDock tool was used. The widely accepted model of amyloid structure assumes that the stacked pleated β-sheets are twisted in such a way that a repeating unit of 24 β-strands constitutes a full helical turn around the fibril axis [45] representing the twist of 15° between the neighboring β-strands [45]. Besides, assuming the heterogeneous nature of amyloid fibrils and the dye ability to display the different binding modes depending on the amyloid fibril structure [46,47], the molecular docking studies were performed using the lysozyme fibrils created with the twisting angles 0°, 5°, 10°, 15° and 20°. The energetically most favourable dye complexes with the fibrillar lysozyme structures are presented in Fig. 1, indicating that all cyanine dyes under study are capable of forming the stable complexes with the lysozyme fibrils.
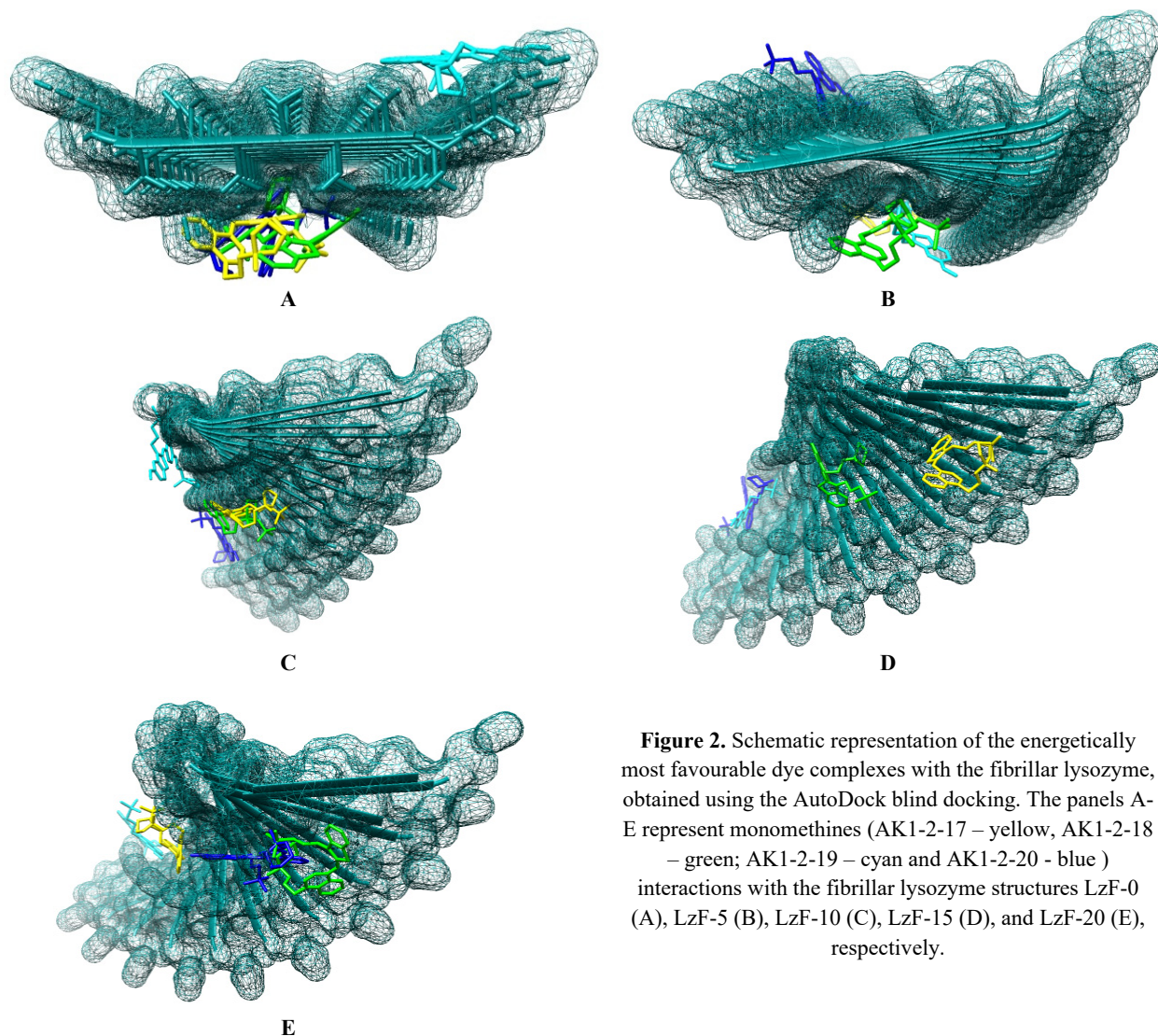
Figure 2. Schematic representation of the energetically most favourable dye complexes with the fibrillar lysozyme, obtained using the AutoDock blind docking. The panels A-E represent monomethines (AK1-2-17 – yellow, AK1-2-18 – green; AK1-2-19 – cyan and AK1-2-20 - blue) interactions with the fibrillar lysozyme structures LzF-0 (A), LzF-5 (B), LzF-10 (C), LzF-15 (D), and LzF-20 (E), respectively.

To characterize the nature of the interactions stabilizing the dye-fibril complex, the protein-ligand interaction profiler PLIP (https://plip-tool.biotec.tu-dresden.de/plip-web/plip/index) was used [42]. It is well- known that the binding of specific probes to amyloid fibrils is governed by various types of intermolecular interactions among which hydrophobic and electrostatic interactions are the main contributors [31,43,46]. The examined monomethine dyes consist of large hydrophobic groups with a cationic charge. Therefore, it might be expected that these dyes interact with the lysozyme amyloid fibril predominantly via hydrophobic interactions. The above assumption was made based on the fact, that the lysozyme amyloid fibrils which were created from the K-peptide of lysozyme (GILQINSRW), contain only the positively charged amino acid residues. For this reason, electrostatic interactions cannot account for the anchoring of fluorophore molecule on the lysozyme fibril surface during the dye-protein complexation. Figure 3 represents the most favorable modes of interactions between the monomethine cyanine dyes and lysozyme amyloid fibrils obtained using the PLIP.

The results obtained with the PLIP server indicate that the dye association with amyloid fibrils LzF-15 is predominantly driven by the hydrophobic dye–protein interactions (dashed grey lines in the Figure 3). More specifically, the monomethine dye AK1-2-17 tends to form the hydrophobic contacts with Asn 16 B, Arg 18 B, Gln 23 C, Asn 25 C, Gln 32 D, Asn 34 D, whereas the AK1-2-18 probe interacts with Asn 52 F, Arg 54 F, Ile 57 G, Gln 59 G, Arg 72 H, Asn 79 I amino acid residues. The binding of the cyanine AK1-2-19 is governed predominantly by hydrophobic interactions between the dye molecule and the lysozyme residues Asn 142 P. Arg 114 P, Gln 149 Q, Asn 151 Q, Arg 153 Q, Gln 158 R, Asn 160 R, Asn 169 S, while the binding of the AK1-2-20 dye is characterized by the hydrophobic contacts with Arg 126 N, Gln 140 P, Asn 142 P, Arg 144 P, Asn 151 Q and Arg 153 Q. The binding affinity for the docked poses was equal to -14.37 kcal/mol (AK1-2-17), -22.16 kcal/mol (AK1-2-18), -20.58 kcal/mol (AK1-2-19) and 17,97 kcal/mol (AK1-2-20). The dye-LzF-15 complexes are additionally stabilized by the hydrogen bonds (blue solid lines in Figure 3) and salt bridges (orange dashed lines). More specifically, the hydrogen bonds were observed between the aliphatic substituents on the nitrogen atom of benzothiazole part of the dye molecules and Gln 14 B (AK1-2-17), Gln 68 N (AK1-2-18), Ser 125 N (AK1-2-19) and Gln 158 R (AK1-2-20) of the lysozyme amyloid fibrils. Moreover, it was found

that the cyanine dyes bearing the methylpyrrolidin group in the quinoline fragment (AK1-2-17, AK1-2-19) form the salt bridges between sulfonic acid in their structure and Arg 27 and Arg 126 amino acid residues, respectively.
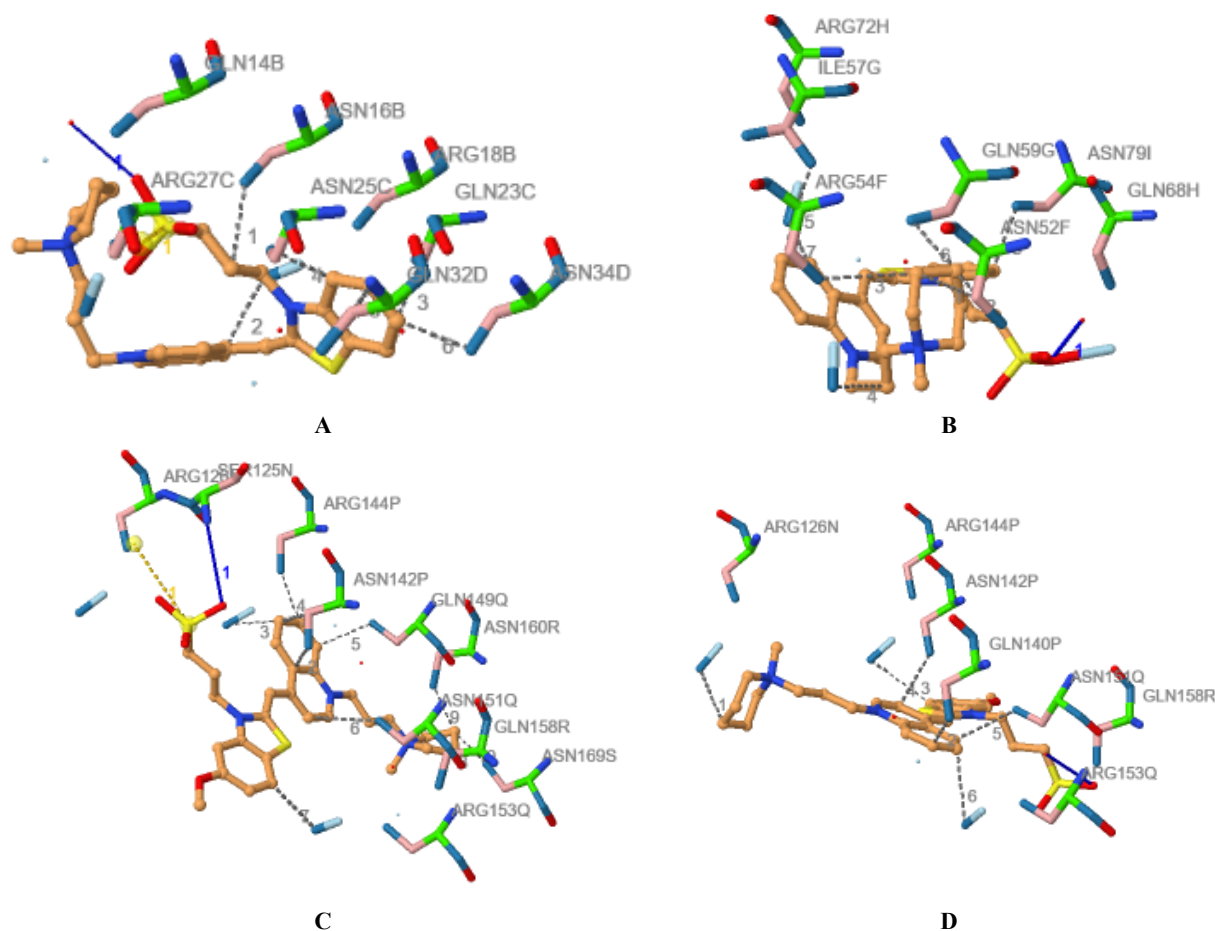

Figure 3. The binding of monomethines (AK1-2-17 – A, AK1-2-18 – B; AK1-2-19 – C and AK1-2-20 - D) to the fibrillar lysozyme analyzed by PLIP. The grey dashed lines represent the hydrophobic interactions between the dye molecules and amino acid residues, while the blue solid and orange dashed lines display the hydrogen bonds and salt bridges, respectively.

Notably, the differences in the cyanine structures as well as in the twisting of the lysozyme fibrils (Table 1) did not significantly affect the mode of cyanine binding. As can be seen in the Table 1, the investigated cyanine dyes interact with the fibril surface (with the aromatic residues on the top of β-sheet or with the edges of the β-sheet). The variation in the cyanine structure and the twisting of amyloid fibrils used for the docking led to the changes in the surrounding amino acid residues involved in the dye-protein complexation, whereas the binding energies remain almost unchanged. Besides, in all docking dye-protein systems we did not observe the insertion of the cyanine dyes into the fibril groove. The above binding mode is the most preferable for the ideal amyloid tracer [23, 25, 43, 46]. Specifically, the highest amyloid-sensing potential was observed for the probes, capable of associating with the superficial grooves of amyloid fibrils [23, 25, 43, 46].

Table 1. The parameters of the dye-fibril complexation predicted by PLIP.

Lysozyme fibril	Hydrophobic interactions	Hydrogen bonds	Salt bridges	Global energy, kcal/mol
AK1-2-17				
LzF-0	Gln 113 , Gln 122 , Asn 124, Arg 126 , Asn 133 , Asn 142	Gln 140	Gln140 - Sulfonicacid	-26.93
LzF-5	Gln 32, Gln 41, Asn 43, Arg 45, Gln 50, Asn 52, Arg 63	Gln 41		-18.42
LzF-10	Gln 95, Asn 97, Gln 104, Gln 113, Arg 117, Gln 122, Asn 124	Gln 95, Ser 107, Gln 113	Arg 108 - Sulfonicacid	-17.89
LzF-15	Asn 16, Arg 18, Gln 23, Asn 25, Gln 32, Asn 34	Gln 14	Arg 27 - Sulfonicacid	-14.37
LzF-20	Asn 88, Arg 90, Asn 97, Arg 99, Asn 106, Asn 115		-	-20.58

AK1-2-18				
LzF-0	Gln 113, Gln 140, Asn 142, Arg 144, Gln 149, Asn 151			-21.03
LzF-5	Gln 113, Asn 115, Gln 131, Arg 135, Gln 140, Asn 142	Gln 113, Gln 131		-22.19
LzF-10	Gln 77, Asn 79, Asn 88, Gln 95, Asn 97, Arg 99, Gln 104, Asn 106		Arg 90 - Sulfonicacid	-24.25
LzF-15	Asn 52 F, Arg 54 F, Ile 57 G, Gln 59 G, Arg 72 H, Asn 79 I	Gln 68		-22.16
LzF-20	Gln 5, Asn 7, Gln 14, Asn 16, Gln 23, Asn 25, Arg 27, Gln 32, Asn 34	Ser 17	Arg 18 - Sulfonicacid	-18.24
AK1-2-19				
LzF-0	Gln 5, Asn 7, Gln 14, Asn 25, Arg 27	Gln 32, Gln 50		-26.62
LzF-5	Asn 52, Asn 61, Gln 68, Asn 70, Arg 72, Asn 79, Agr 81		Arg 108- Sulfonicacid	-20.91
LzF-10	Arg 72, Gln 77, Gln 86, Asn 88, Asn 97, Arg 117 M	Trp 118, Gly 119	Gln 68 - Sulfonicacid	-16.55
LzF-15	Asn 142. Arg 114, Gln 149, Asn 151, Arg 153, Gln 158, Asn 160, Asn 169	Ser 125	Arg 126 - Sulfonicacid	-20.58
LzF-20	Asn 133, Asn 151, Arg 153			-16.94
AK1-2-20				
LzF-0	Asn 79, Arg 81, Gln 86, Asn 88, Asn 97	Gln 68		-18.16
LzF-5	Asn 61, Arg 63, Gln 68, Asn 70, Asn 79, Arg 81	Gln 50	Arg 54- Sulfonic acid	-20.29
LzF-10	Asn 34 D, Arg 36 D, Gln 41 E, Gln 50 F, Asn 52 F, Arg 63 G	GLn 59		-17.16
LzF-15	Arg 126, Gln 140, Asn 142, Arg 144, Asn 151, Arg 153	Gln 158		-17.97
LzF-20	Asn 16, Arg 18, Gln 23, Gln 32, Asn 34, Arg 36, Asn 43, Arg 45	Gln 41, Gln 50	Arg 63- Sulfonic acid	-19.16

In this context, it should be noted that insertion of many cyanine dyes into fibril grooves can also be driven by electrostatic (along with hydrophobic, H-bonds, π-stacking) dye-protein interactions [24, 31, 46]. However, the amyloid fibrils from the K-peptide of lysozyme (GILQINSRW) contain only the positively charged amino acid residues, while the dyes under study are also cationic in nature. Therefore, we expect that significant variations in the docking results may appear using amyloid fibrils created with other amino-acid sequences. Overall, the docking results presented here can be regarded as a starting point for elucidating the nature of cyanine-fibril binding that is important for the development and optimization of the fluorescent probes for amyloid fibril detection.

CONCLUSIONS

To summarize, in the present study the molecular docking technique was used to investigate the interactions between the novel monomethine cyanine dyes and the model amyloid fibrils of lysozyme. Using the AutoDOCK and the protein-ligand interaction profiler PLIP it was found that: i) the monomethines do not insert in the fibril groves and interact with the fibril surface; ii) the dye-fibril binding is governed by the hydrophobic interactions, salt bridges and hydrogen bonds between the aliphatic substituents on the nitrogen atom of benzothiazole part of the dye molecules and боковими залишками амінокислот; iii) the variations in the cyanine structure and in the lysozyme fibril twisting do not significantly influence the binding mode of cyanines under study. Overall, the obtained results can be useful for extending the application of cyanine dyes to amyloid fibril sensing.

ORCID IDs
Olga Zhytniakivska, https://orcid.org/0000-0002-2068-5823; **Uliana Tarabara,** https://orcid.org/0000-0002-7677-0779
Atanas Kurutos, https://orcid.org/0000-0002-2068-5823; **Kateryna Vus,** https://orcid.org/0000-0003-4738-4016
Valeriya Trusova, https://orcid.org/0000-0002-7087-071X; **Galyna Gorbenko,** https://orcid.org/0000-0002-0954-5053

REFERENCES
[1] J. Fan, A. Fu, and L. Zhang, Quant. Biol. **7(2)**, 83-89 (2019). https://doi.org/10.1007/s40484-019-0172-y
[2] T. Lengauer, and M. Rarey, Cur. Opin. Struct. Biol. **6**, 402-406 (1996). https://doi.org/10.1016/S0959-440X(96)80061-3

[3] N.S. Pagadala, K. Syed, and J. Tuszynski, Biophys Rev. **9**, 91-102 (2017), https://doi.org/10.1007/s12551-016-0247-1

[4] P.H.M. Torres, A.S.R. Sodero, P. Jofily, F.P. Silva-Jr, Int. J. Mol. Sci. **20**, 4574 (2019). https://doi.org/10.3390/ijms20184574

[5] L.G. Ferreira, R.N. Dos Santos, G. Oliva, and A.D. Andricopulo, Molecules, **20(7)**, 13384-13421 (2015). https://doi.org/10.3390/molecules200713384

[6] W. Yu, and A.D. MacKerell Jr. Antibiotics, **1520**, 85-106 (2016). https://doi.org /10.1007/978-1-4939-6634-9_5

[7] J. Ritu, D. Mehak, K. Alka, and C. Anil K., Cur. Bioinform. **15**, 270-278 (2020). https://doi.org/10.2174/1574893615666191219094216

[8] J.A. Pradeepkiran, and P.H. Reddy, Cells, **8**, 260 (2019). https://doi.org/10.3390/cells8030260

[9] R. Yu, L. Chen, R. Lan, R. Shen, and P. Li, Int. J. Antimicrob. Agents, **56**, 106012 (2020). https://doi.org/10.1016/j.ijantimicag.2020.106012

[10] S. Das, S. Sarmah, S. Lyndem, and A.S. Roy, J. Biomol. Struct. Dyn. **39**, 3347-3357 (2021). https://doi.org/10.1080/07391102.2020.1763201

[11] D.R. Langley, A. W. Walsh, C. J. Baldick, et al, J, Virol. **81**, 3992-4001 (2007). https://doi.org/10.1128/JVI.02395-06

[12] W.-G. Gu, X. Zhang, and J.-F. Yuan. The AAPS J. **16**, 674-680 (2014). https://doi.org/10.1208/s12248-014-9604-9

[13] I. Ali, M.N. Lone, and H.Y. Alboul-Enein. Med Chem Comm. **9**, 1742-1773 (2017). https://doi.org/10.1039/C7MD00067G

[14] T. Al-Warhi, A. Sabt, E.B. Elkaeed, and W.M. Eldehna. Bioorg. Chem. https://doi.org/10.1016/j.bioorg.2020.104163

[15] A. Fisher, B.G. Freedman, D.R. Bevan, and R.S. Senger. Comput. Struct. Biotechnol. J. **11**, 91-99 (2014). https://doi.org/10.1016/j.csbj.2014.08.010

[16] H.Liu, M. Tu, S. Cheng, H. Chen, Z. Wang, and M. Du. Food Funct. **10**, 886-896 (2019). https://doi.org/10.1039/C8FO02235F

[17] A. Chakraborty, A.K. Panda, R. Ghosh, and A. Biswas, Arch. Biochem. Biophys. **665**, 107-113 (2019). https://doi.org/10.1016/j.abb.2019.03.001

[18] A. Mukherjee, and B. Singh, J. Luminesc. **190**, 319-327 (2017). https://doi.org/10.1016/j.jlumin.2017.05.068

[19] T. Pantsar, and A. Poso, Molecules. **23**, 1899 (2018). https://doi.org/10.3390/molecules23081899

[20] R. Wang, L. Lai, and S. Wang, J. Comput. Aided Mol **16**, 11-26 (2002). https://doi.org/10.1023/A:1016357811882

[21] S. Ghasemzadeh, and G.H. Riazi, Int. J. Biol. Macromol. **154**, 1505-1516 (2020). https://doi.org/10.1016/j.ijbiomac.2019.11.032

[22] Z. Chen, G. Krause, and B. Reif, J. Mol. Biol. **354**, 760-776 (2005). https://doi.org/10.1016/j.jmb.2005.09.055

[23] N.H. Mudliar, and P.K. Singh, Chem. Commun. **55**, 3907-3910 (2019). https://doi.org/10.1039/C9CC01262A

[24] A.K. Mora, P.K. Singh, B.S. Patro, and S. Nath, Chem. Commun. **52**, 12163-12166 (2016). https://doi.org/10.1039/C6CC05600H

[25] O. Zhytniakivska, A. Kurutos, U. Tarabara, et al. J. Mol. Liq. **311**, 113287 (2020). https://doi.org/10.1016/j.molliq.2020.113287

[26] G.Q. Gao, and A.W. Xu, RSC Adv. **3**, 21092-21098 (2013). https://doi.org/10.1039/C3RA43259A

[27] R. Sabate, and J. Estelrich, Biopolymers, **72**, 455-463 (2003). https://doi.org/10.1002/bip.10485

[28] H.L. Yang, S.Q. Fang, Y.W. Tang, et al. Eur. J. Med. Chem. **179**, 736-743 (2019). https://doi.org/10.1016/j.ejmech.2019.07.005

[29] X. Wang, H.N. Chan, N. Desbois, C.P. Gros, et al. ACS. Appl. Mater. Interfaces, **13**, 18525-18532 (2021). https://doi.org/10.1021/acsami.1c01585

[30] T. Smidlehner, H. Bonnet, S. Chierici, and I. Piantanida, Bioorg. Chem. 104196 (2020). https://doi.org/10.1016/j.bioorg.2020.104196

[31] K. Vus, M. Girych, V. Trusova, et al. J Mol Liq, **276**, 541-552 (2019). https://doi.org/10.1016/j.molliq.2018.11.149

[32] V. Kovalska, M. Losytskyy, V. Chernii, K. Volkova, et al. Bioorg. Med. Chem. **20**, 330-334. (2012). https://doi.org/10.1016/j.bmc.2011.10.083

[33] S. Chernii, Y. Gerasymchuk, M. Losytskyy, et al. PLOS ONE, **16**, e0243904. (2021). https://doi.org/10.1371/journal.pone.0243904

[34] V. Trusova, East Eur. J. Phys. **2**, 51-58 (2015). https://doi.org/10.26565/2312-4334-2015-2-06

[35] D. Schneidman-Duhovny, Y. Inbar, R. Nussimov, and H. Wolfson, Nucl. Acids Res. **33**, W363-W367 (2006). https://doi.org/10.1093/nar/gki481

[36] N. Andrusier, R. Nussimov, and H. Wolfson. Proteins, **69**, 139-159 (2007). https://doi.org/10.1002/prot.21495

[37] M.R. Smaoui, F. Poitevin, M. Delarue, et al. Biophys J. **104**, 139-159 (2007). https://doi.org/10.1016/j.bpj.2012.12.037

[38] S. Dallakyan, and A.J. Olson, Methods Mol. Biol. **1263**, 243-250 (2015). https://doi.org/10.1007/978-1-4939-2269-7_19

[39] P. Csizmadia, In: *Proceedings Of ECSOC-3, The Third International Electronic Conference on Synthetic Organic Chemistry*, 367-369 (1999). https://doi.org/10.3390/ECSOC-3-01775

[40] M.D. Hanwell, D.E. Curtis, D.C. Lonie, T. Vandermeersch, E. Zurek, and G.R. Hutchison, J. Cheminform. **4**, 17 (2012). https://doi.org/10.1186/1758-2946-4-17

[41] E.F. Pettersen, T.D. Goddard, C.C. Huang, G.S. Couch, D.M. Greenblatt, E.C. Meng, and T.E. Ferrin. J. Comput. Chem. **25**, 1605-1612 (2004). https://doi.org/10.1002/jcc.20084

[42] S. Salentin, S. Schreiber, V. Joachim Haupt, M.F. Adasme, and M. Schroeder, Nucleic Acids Res. **43** W443-W447 (2015). https://doi.org/10.1093/nar/gkv315

[43] M. Biancalana, and S. Kode, Biochem. Biophys. Acta, **1804**, 1405-1412 (2010). https://doi.org/10.1016/j.bbapap.2010.04.001

[44] E.F. Marondedze, K.K. Govender, and P.P. Govender, Biophys Chem. **256**, 106281 (2020). https://doi.org/10.1016/j.bpc.2019.106281

[45] M. Sunde, L. Serpell, M. Bartlam, et al. J. Mol. Biol. **273**, 729-739 (1997). https://doi.org/10.1006/jmbi.1997.1348

[46] O. Zhytniakivska, A. Kurutos, M. Shchuka, et al. Chem Phys Lett, **785**, 139127 (2021). https://doi.org/10.1039/D1CP01359A

[47] A. Sulatskaya, N. Rodina, M. Sulatsky, et al. Int. J. Mol. Sci. **19**, 2486 (2018). https://doi.org/10.3390/ijms19092486

МОЛЕКУЛЯРНИЙ ДОКІНГ МОНОМЕТИНОВИХ ЦІАНІНОВИХ БАРВНИКІВ З АМІЛОЇДНИМИ ФІБРИЛАМИ ЛІЗОЦИМУ

О. Житняківська[a], У. Тарабара[a], А. Курутос[b,c], К. Вус[a], В. Трусова[a], Г. Горбенко[a]

[a]Кафедра медичної фізики та біомедичних нанотехнологій, Харківський національний університет імені В.Н. Каразіна
м. Свободи 4, Харків, 61022, Україна
[b]Інститут органічної хімії та фітохімії Академії Наук Болгарії, вул. Акад. Бончева, 9, 1113, Софія, Болгарія
[c]Кафедра фармацевтичної та прикладної органічної хімії, Факультет хімії та фармації
Софійський університет імені Св. Климента Охридського, 1164, Софія, Болгарія

Агрегація білків у високовпорядковані супрамолекулярні агрегати є ознакою багатьох захворювань людини, включаючи неврологічні розлади (хвороби Паркінсона, Альцгеймера та Хантінгтона), діабет ІІ типу, системний амілоїдоз, енцефалопатію, тощо. Самий простий і ефективний метод детектування та характеризації амілоїдних фібрил in vitro та візуалізації амілоїдних включень in vivo базується на використанні зондів, чутливих до бета-складчастих мотивів. Для створення нових амілоїд-специфічних барвників і оптимізації уже існуючих сполук, важливо розуміти на молекулярному та атомному рівнях механізми їх взаємодії у центрах зв'язування. Одним із особливо потужних методів, здатних забезпечити розуміння механізмів різних типів біомолекулярних взаємодій на атомному рівні, є метод молекулярного докінгу. У даній роботі метод молекулярного докінгу використовувався для дослідження взаємодії між монометиновими ціаніновими барвниками та модельними амілоїдними фібрилами, що були побудовані з К-пептиду лізоциму GILQINSRW (залишки 54–62 білка дикого типу). За допомогою програмного інтерфейсу AutoDOCK і профайлера білок-лігандної взаємодії PLIP встановлено: 1) монометини взаємодіють з поверхнею фібрили (з ароматичними залишками на вершині β-листа або з краями β-листа); ii) зв'язування барвників відбувається за рахунок гідрофобних взаємодій, сольових містків та водневих зв'язків між аліфатичними замісниками на атомі азоту бензотіазолової частини молекули барвника та амілоїдної фібрили лізоциму; iii) варіації в структурі ціанінів та в ступені скручування амілоїду лізоциму суттєво не впливають на характер взаємодії барвників з фібрилами.
Ключові слова: монометинові ціанінові зонди, амілоїдні фібрили лізоциму, молекулярний докінг

SAMPLE PREPARATION FOR THE EFFECTIVE ACCUMULATION AND DETECTION OF THE BETA-ACTIVE Rn-222 DECAY PRODUCTS[†]

Gennadiy Onyshchenko[a,b,*], Ivan Yakymenko[a], Oleksandr Shchus[a], Anatoliy Lokha[c]

[a]Karazin Kharkiv National University, 4 Svobody Sq., Kharkov, 61022, Ukraine
[b]Institute for Scintillation Materials, STC "Institute for Single Crystals", National Academy of Sciences of Ukraine
60 Nauky Ave., 61001 Kharkiv, Ukraine
[c]Hryhoriy Skovoroda University in Pereyaslav, 08401, Pereyaslav, Kyiv Region, Ukraine
*Corresponding Author: gennadiy.m.onyshchenko@karazin.ua
Received July 1, 2022; revised August 12, 2022; accepted August 29, 2022

The sample preparation method and the results of experimental measurements of the concentration of beta-radioactive aerosols (the decay products of Radon-222 in the air) are presented. The experimental equipment includes an electrostatic aerosol collector and a time spectrometer based on the PMT with a plastic scintillator. The accumulation of aerosols on the foil lasted for about 12 hours. The activity of accumulated aerosols was measured in the time interval of 0 to 300 minutes. The use of the time analyzer spectrometer, the proposed aerosol accumulator and the method of processing the accumulated spectrum makes it possible to increase the sensitivity of the radiometer in comparison with the collection method based on air filters. Applying the time-spectrum development procedure to the constituent components makes it possible to reliably establish the connection of aerosols registered in the room with β-active decay products of radon-222: Po-218, Pb-214, Bi-214.
Keywords: Radon-222; beta – activity, decay, electrostatic methods, sample preparation
PACS: 87.66.-a, 23.60.+e, 23.40.-s, 89.40.Dd, 29.40.-n, 07.88.+y

Radioactive aerosols are a mixture of dust and radioactive particles, which are α-, β- and γ emitters. Decay products of Rn-222, $T_{1/2}$ = 3.823 days; Rn-220, $T_{1/2}$ = 0.9267 min; Rn-219, $T_{1/2}$ = 3.96 s and their daughter products – Po-218, $T_{1/2}$ = 3.167 min; Pb-214, $T_{1/2}$ = 26.833 min; Bi-214, $T_{1/2}$ = 19.833 min are deposited on particles suspended in the air. Radon continuously enters the atmosphere from terrestrial rocks: Rn-222 - during the alpha decay of Ra-226 nuclei (uranium-radium family), and Rn-220 – during the alpha decay of Ra-224 nuclei [1]. The Rn-222 isotope gives approximately 50-55% of the effective radiation dose every Earth inhabitant receives annually. The Rn-220 isotope adds another ~ 5-10% to this [1].

No less dangerous are the decay products of radon - beta-radioactive isotopes of lead, bismuth, and polonium, since they form aerosols that when they enter the human lungs and cause micro burns.

The combination of the developed method of analysis and electrostatic aerosol accumulator and time analysis of the sample activity makes it possible to associate aerosols recorded in a room with β-active decay products of radon-222. It also increases the reliability of recording Rn-222 and significantly reduces the measurement time compared, for example, with a technique based on the use of CR-39 films [2].

The references have known methods for assessing the radioactivity of aerosols - radon decay products by measuring gamma and beta radiation [3-5]. In these works, the registration of radon decay products is carried out, as a rule, using spectrometric amplitude analysis. The use of multilayer filters in the registration of beta aerosols is not effective enough because, simultaneously with the accumulation, the outflow of accumulated particles occurs.

In work [6] was used a two-electrode filter, which provides for the capture of radon beta- products, is considered but does not allow obtained a high sensitivity. The paper [7] considered the approach of direct deposition of decay products on the spherical surface of the Si detector. The potential on the surface is -3 kV. The concentration of aerosols and the sample activity are not high; the data accumulation and processing speed are also low. In [8] work is represented a multilayer filter for collecting aerosols. The air in the room was blown through a filter, allowing radon decay products to accumulate. The method's efficiency is low due to the complexity of sample preparation for analysis and the low efficiency of the blowing way.

SAMPLE PREPARATION AND MEASUREMENT TECHNIQUE

Reliable registration of radon isotopes and decay products [2] for gas mixture is an unfinished problem. Mainly significant difficulties are determined the low adsorption of radon by the filters. For the quantity determined of radon isotopes, it is also necessary to have radioactive gas samples. Their creation is significantly complex, especially for the long-term isotope - radon-222. The decay products, being positively charged, can be subject to electrostatic precipitation. The alpha particle escapes produce the positive charge of the ionization of the atomic shell. It is also possible to have ionization by the kinetic energy of the recoiled atomic nucleus. To accumulate the radioactive sample was used an

electrostatic method. On a sheet of aluminum foil (~ 0.02 mm) with an area of ~ 1 m^2, which was placed on a horizontally stretched insulating thread, a potential of mines 1500 V was applied. The time exposure was 12 hours. Due to the difference in the potentials of the dust particles in the air and the filter (foil), it was possible to deposit the aerosols efficiently. After the exposure, the foil sheet was reduced to a cylinder, Ø5x0.2cm. The additional reduction of the sample allows us to significantly increase the concentration of radioactive particles per unit area of the scintillation detector. Fig. 1 shows a circuit of a voltage converter used for an electrostatic filter. Fig. 2 shows a detector part of the measurement setup.
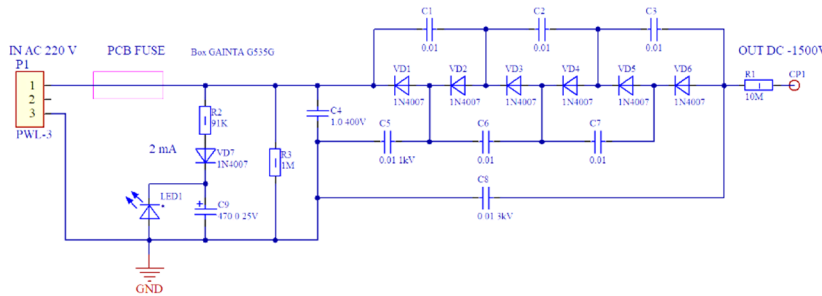

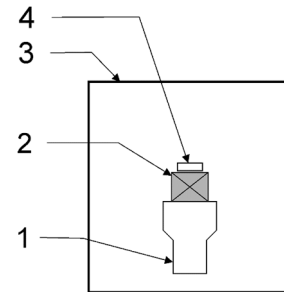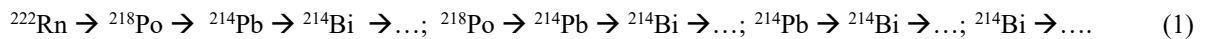**Figure 1**. Power supply for an electrostatic filter

Figure 2. Detector system. 1 – PMT R1307 Hamamatsu, 2 – UPS-923A plastic detector, 3 – lead background shield, 4 – probe sample

RESULTS AND MEASUREMENTS

In this work, it was assumed that the activity of particles in the indoor air aerosol collected on the filter is mainly determined by the decay products of the isotope of radon: Rn-222 (T$_{1/2}$=3.82 days). The contribution of other isotopes – Rn-220 (T$_{1/2}$ = 55.6 s), Rn-219 (T$_{1/2}$ = 3.96 s) was neglected due to the short half-life compared to Rn-222 and lower prevalence. It was assumed that possible isotopes that were in the room and got on the radiometer filter and then disintegrated during the measurement process are isotopes Rn-222, Po-218, Pb-214 and Bi-214:

$$^{222}\text{Rn} \rightarrow {}^{218}\text{Po} \rightarrow {}^{214}\text{Pb} \rightarrow {}^{214}\text{Bi} \rightarrow \ldots; \quad {}^{218}\text{Po} \rightarrow {}^{214}\text{Pb} \rightarrow {}^{214}\text{Bi} \rightarrow \ldots; \quad {}^{214}\text{Pb} \rightarrow {}^{214}\text{Bi} \rightarrow \ldots; \quad {}^{214}\text{Bi} \rightarrow \ldots. \tag{1}$$

The decay of isotopes accumulated in the filter is described by the following system of equations:

$\dfrac{dN_1}{dt} = -\lambda_1 N_1$ 	– decay of the accumulated products on the filter ^{222}Rn (N_1)

$\dfrac{dN_2}{dt} = \lambda_1 N_1 - \lambda_2 N_2$ 	– production ^{218}Po (N_2) from decay of ^{222}Rn (N_1) and decay of the accumulated products on the filter (N_2)

$\dfrac{dN_3}{dt} = \lambda_2 N_2 - \lambda_3 N_3$ 	– production of the ^{214}Pb (N_3) from decays of ^{218}Po (N_2), ^{222}Rn (N_1) and decay of the accumulated products on the filter ^{214}Pb (N3)

$\dfrac{dN_4}{dt} = \lambda_3 N_3 - \lambda_4 N_4$ 	– production ^{214}Bi (N_4) from decays of the ^{214}Pb (N_3), ^{218}Po (N_2), ^{222}Rn (N_1) and decay of the accumulated products on the filter ^{214}Bi (N_4)

$$\tag{2}$$

where N_1, N_2, N_3, N_4 – quantity of the radioactive nuclei ^{222}Rn, ^{218}Po, ^{214}Pb, ^{214}Bi respectively.

The activity of the source A can be related to the number of radioactive nuclei N and the detector efficiency ε as follows: $(-dN/dt) = A$; $(-dN/dt) \cdot \varepsilon = \lambda \cdot N \cdot \varepsilon = A \cdot \varepsilon$. In the calculation was assumed that $\varepsilon = 1$.

The change over time in the total activity of the isotopes accumulated on the filter could be described by the system of the following equations:

– decay of the accumulated products on the filter ^{222}Rn ($N_1(0)$):

$$N_1(t) = N_1(0)e^{-\lambda_1 t}, \tag{3}$$

– production ^{218}Po from the decay ^{222}Rn, and decay of the accumulated products on the filter ^{218}Po ($N_2(0)$):

$$N_2(t) = \frac{\lambda_1 N_1(0)}{(\lambda_2 - \lambda_1)}\left[e^{-\lambda_1 t} - e^{-\lambda_2 t}\right] + N_2(0)e^{-\lambda_2 t}, \tag{4}$$

– production ^{214}Pb from the decay ^{218}Po, ^{222}Rn, and decay of the accumulated products on the filter ^{214}Pb ($N_3(0)$):

$$N_3(t) = \frac{\lambda_2 \lambda_1 N_1(0)}{(\lambda_2 - \lambda_1)}\left[\frac{e^{-\lambda_1 t} - e^{-\lambda_3 t}}{(\lambda_3 - \lambda_1)} - \frac{e^{-\lambda_2 t} - e^{-\lambda_3 t}}{(\lambda_3 - \lambda_2)}\right] + \frac{\lambda_2 N_2(0)}{(\lambda_3 - \lambda_2)}\left(e^{-\lambda_2 t} - e^{-\lambda_3 t}\right) + N_3(0)e^{-\lambda_3 t}, \tag{5}$$

– production ^{214}Bi from the decay ^{214}Pb, ^{218}Po, ^{222}Rn, and also decay of the accumulated products on the filter ^{214}Bi ($N_4(0)$):

$$N_4(t) = \frac{\lambda_3\lambda_2\lambda_1 N_1(0)}{(\lambda_2-\lambda_1)}\left[\frac{1}{(\lambda_3-\lambda_1)}\left(\frac{e^{-\lambda_1 t}-e^{-\lambda_4 t}}{(\lambda_4-\lambda_1)}-\frac{e^{-\lambda_3 t}-e^{-\lambda_4 t}}{(\lambda_4-\lambda_3)}\right)-\frac{1}{(\lambda_3-\lambda_2)}\left(\frac{e^{-\lambda_2 t}-e^{-\lambda_4 t}}{(\lambda_4-\lambda_2)}-\frac{e^{-\lambda_3 t}-e^{-\lambda_4 t}}{(\lambda_4-\lambda_3)}\right)\right] +$$
$$+ \frac{\lambda_3\lambda_2 N_2(0)}{(\lambda_3-\lambda_2)}\left[\frac{e^{-\lambda_2 t}-e^{-\lambda_4 t}}{(\lambda_4-\lambda_2)}-\frac{e^{-\lambda_3 t}-e^{-\lambda_4 t}}{(\lambda_4-\lambda_3)}\right]+\frac{\lambda_3 N_3(0)}{(\lambda_4-\lambda_3)}\left(e^{-\lambda_3 t}-e^{-\lambda_4 t}\right)+ \quad N_4(0)e^{-\lambda_4 t}. \tag{6}$$

Figure 3. shows the results of the analysis of the activity of the sample (analysis time 300 min.), accumulated on the filter for a time interval of 12 hours using the system of equations (3-6).

The total activity of aerosols was measured in a closed room on the 1st floor of the building. The time of collecting aerosol particles by the electrostatic method was 12 hours. After installing the filter on the scintillation counter (detector - plastic), the change in the total beta activity of the filter was recorded duration 300 minutes, and the time of the accumulation of one channel was 1 minute. The time spectrometer was used from [8].
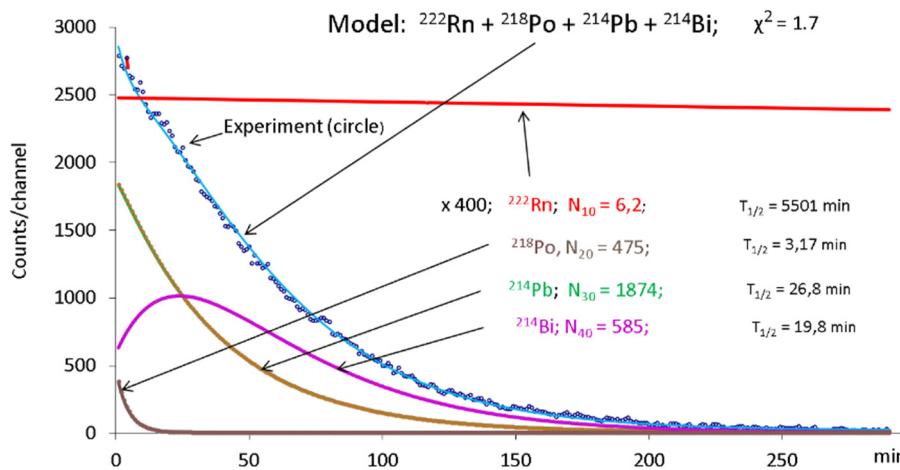

Figure 3. Results of processing the counts (counts/channel) of the decay products of the measured sample. The event pulse recorded by the detector is plotted along the vertical axis. N_{i0} – calculated initial values (activities) for beta-components

The analysis of the decay curve and determination of the initial activities of the components is performed by approximating the experimental data of the theoretical curve, which is the sum of the calculated activities on the aluminum foil ($N_1(t)$, ^{222}Rn) + ($N_2(t)$, ^{218}Po) + ($N_3(t)$, ^{214}Pb) + ($N_4(t)$, ^{214}Bi) duration 300 minutes.

Fit quality criterion is:

$$\chi^2 = \frac{1}{n-5}\sum_1^n\left(\frac{N_{exp}-N_{th}}{\delta i(N_{exp})}\right)^2, \tag{7}$$

where n – the number of experimental points form a decay curve; N_{exp} – registered counts (activities); $\delta_i(N_{exp})$ – absolute error of a single measurement, $\delta_i = \sqrt{N_{i,exp}}$.

During the fitting, the initial activities of N_1, N_2, N_3 and N_4 was varied. As a result, the following values of the initial activities of beta-active components on the filter were obtained: $A_{10} = N_1(0)$ (^{222}Rn) = 6.2; $A_{20} = N_2(0)$ (^{218}Po) = 475; $A_{30} = N_3(0)$ (^{214}Pb) =1874; $A_{40} = N_4(0)$ (^{214}Bi) = 585. The relative error of approximation, estimated based on the root-mean-square error (RMS) of the spectrum by expression (8) was 4.5%, $\chi^2 = 1.7$.

$$\delta_{\bar{x}} = \frac{1}{(\sum_1^n N_{i,exp})/n}\sqrt{\frac{1}{n-1}\sum_1^n\left(N_{i,exp}-N_{i,th}\right)^2}, \tag{8}$$

RESULTS AND DISCUSSION

The results of the measurements and the analysis of the decay curves indicate the presence in the filter (Al-foil) of the alpha-active isotope of radon Rn-222, beta-active products of decay of radon - Pb-214, Po -218 and Bi-214. The ratio of initial activities of Pb-214 / Bi-214 for the studied room was 3.2:1.

The presence of Rn-222 alpha emitters in the filter leads to a noticeable improvement in the agreement between the model and experimental curves. An exception to the analysis of the Rn-222 isotope worsens the quality of the fit, with the value of $\chi^2 = 6.5$, RMS = 6.7%. Thus, the analysis results (χ^2 values, activity values of the components) indicate that the activity of aerosols accumulated in the filter is formed mainly by beta-active products of the decay of the radon isotope Rn-222.

CONCLUSIONS

The results of measurements and processing confirm a significant increase in the sensitivity of the method due to the proposed electrostatic method of the sample preparation and an increase in the reliability of measurements due to the use of time analysis of the decay curve and a scintillation counter.

Application of the proposed technique allows to reduce a sample accumulation time of ~ 12 hours and a processing time of ~ 5 hours to obtain a statistical error of fitting ~ 4.5%.

ORCID IDs
Ⓘ**Gennadiy Onyshchenko**, https://orcid.org/0000-0001-6945-8413; Ⓘ**Ivan Yakymenko**, https://orcid.org/0000-0002-0194-8376
Ⓘ**Oleksandr Shchus'**, https://orcid.org/0000-0001-6063-197X; Ⓘ**Anatoliy Lokha,** https://orcid.org/0000-0002-4219-8970

REFERENCES
[1] I. Grigoriev, E. Meilikhov, and A. Radzig, *Handbook of Physical Quantities*, 1996.
[2] S.A. Durrani, and R.K. Bull, Chapter 2 - Interactions of Charged Particles with Matter, in: *Solid State Nuclear Track Detection*, edited by S.A. Durrani, and R.K. Bull, (Pergamon, 1987), pp. 13-22. https://doi.org/10.1016/B978-0-08-020605-9.50006-X
[3] P. Jovanovic, Radon exhalation rate measurements on and around the premises of a former coal mine, Science of The Total Environment, **272**(1–3), 147 (2001), https://doi.org/10.1016/S0048-9697(01)00681-7
[4] D. Austen, and W. Brouwer, Radioactive balloons: experiments on radon concentration in schools or homes, Physics Education, **32**(2), 97 (1997). https://doi.org/10.1088/0031-9120/32/2/016
[5] L. Yuan, S. Geng, B. Luo, J. Wu, and J. Wang, Yuan, in: *Proceedings of the 2016 International Forum on Energy, Environment and Sustainable Development*, (Atlantis Press, 2016). https://doi.org/10.2991/ifeesd-16.2016.5
[6] F. Mamedov, P. Čermák, J. Jakůbek, K. Smolek, I. Štekl, and J. Vlášek, Journal of Instrumentation, **8**, C03011 (2013). https://doi.org/10.1088/1748-0221/8/03/C03011
[7] S.-Y. Chang, C.-W. Ha, and B.-H. Lee, "Measurement of Radon-222 Exhalation Rate from Building Materials by Using CR-39 Radon Cup", Journal of Radiation Protection, **16**(1), (1991). https://www.jrpr.org/upload/pdf/BSBOB5_1991_v16n1_15.pdf
[8] I.I. Yakimenko, N.G. Styervoyedov, A.F. Shchus, and G.M. Onyshchenko, Radon-222 Detection Using Beta-Decay Products, East Eur. J. Phys. **3**(2), 65 (2016). https://doi.org/10.26565/2312-4334-2016-2-09

ПІДГОТУВАННЯ ПРОБ ДЛЯ ЕФЕКТИВНОГО НАКОПИЧЕННЯ ТА РЕЄСТРАЦІЇ БЕТА-АКТИВНИХ ПРОДУКТІВ РОЗПАДУ Rn-222
Геннадій Онищенко[a,b], Іван Якименко[a], Олександр Щусь[a], Анатолій Лоха[c]
[a]Харківський національний університет імені В.Н. Каразіна, м. Свободи 4, 61022, Харків, Україна
[b]Інститут сцинтиляційних матеріалів, НТЦ «Інститут монокристалів», НАН України
пр. Науки, 60, 61001 м. Харків, Україна
[c]Університет Григорія Сковороди в Переяславі, 08401, м. Переяслав, Україна

Представлена методика підготування проб та результати вимірювань концентрації бета-радіоактивних аерозолів - продуктів розпаду Радону-222 у повітрі. До складу експериментального тракту входять електростатичний збирач аерозолів та сцинтиляційний часовий спектрометр на базі ФЕП з пластиковим сцинтилятором. Накопичення аерозолів на фользі тривало близько 12 годин. Вимірювання активності накопичених аерозолів проводилося в інтервалі 0-300 хвилин. Використання часового аналізатора, запропонованого накопичувача аерозолів і методу обробки накопиченого спектра дає змогу суттєво підвищити чутливість радіометра у порівнянні з методикою збору на основі повітряних фільтрів. Застосування процедури розвинення часового спектра на складові компоненти дає змогу надійно встановлювати зв'язок зареєстрованих в приміщенні аерозолів з β-активними продуктами розпаду радону-222: Po-218, Pb-214, Bi-214.
Ключові слова: Радон-222; бета-активність, розпад, електростатичний метод, підготування проб

INSTRUCTIONS FOR PREPARING MANUSCRIPT IN THE EAST EUROPEAN JOURNAL OF PHYSICS

Nikita F. Author[a],*, Peter V. Co-Author(s)[b],†

[a]Affiliation of first author
[b]Affiliation of second author (if different from the first Author)
*Corresponding Author: corresponding_authors@mail.com, [a]ORCID ID
†E-mail: co_authors@mail.com, [b]ORCID ID

Each paper must begin with an abstract. The abstract should be typed in the same manner as the body text (see below). Please note that these Instructions are typed just like the manuscripts should be. The abstract must have at least **1800 phonetic symbols (about 250-300 words)**, supplying general information about the achievements, and objectives of the paper, experimental technique, methods applied, significant results and conclusions. Page layout: the text should be printed on the paper **A4** format, at least **5 pages**, with margins of: **Top - 3, Bottom, Left and Right - 2 cm**. The abstract, keywords should be presented **in English** (only for foreign authors), **and Ukrainian**.
Keywords: there, must, be, 5-10 keywords
PACS: specify PACS code(s) here

This is **Introduction** section. This paper contains instructions for preparing the manuscripts. The text should be prepared in "**doc"** or **"docx"** format.

INSTRUCTIONS

The text should be typed as follows:
- **title**: Times New Roman, 12 pt, ALL CAPS, bold, 1 spacing, centred;
- **authors**: name, initials and family names; Times New Roman, 12 pt, bold, 1 spacing, centred;
- **affiliation(s)**: Times New Roman, 9 pt, italic, 1 spacing, centred;
- **abstract**: Times New Roman, 9 pt, 1 spacing, justified;
- **body text**: Times New Roman, 10 pt, 1 spacing, justified; paragraphs in sections should be indented right (tabulated) for 0.75 cm;
- **section titles**: Times New Roman, 10 pt, bold, 1 spacing, centred, without numbering, one line should be left, blank above section title;
- **subsection titles**: Times New Roman, 10 pt, bold, 1 spacing, centred, without numbering in accordance to the section (see below), one line should be left blank above subsection title;
- **figure captions**: width of the figure should be 85 or 170 mm, Figures should be numbered (**Figure 1**.) and titled below Figures using sentence format, Times New Roman, 9 pt, 1 spacing, centred (if one line) or justified (if more than one line); one line should be left blank below figure captions;
- **table captions**: width of the table should be 85 or 170 mm, tables should be numbered (**Table 1.**) and titled above tables using sentence format, Times New Roman, 10 pt, 1 spacing, justified, Tables should be formatted with a single-line box around the outside border and single ruling lines between rows and columns; one line should be left blank below tables;
- **equations**: place equations centred, numbered in Arabic: (1), the number is aligned to the right; equations should be specially prepared in **MathType** or "**Microsoft Equation"**, Times New Roman, 10 pt, one line should be left blank below and above equation.

Additional instructions

Numerated figures and tables should be embedded in your text and placed after they are cited. Only sharp photographs and drawings are acceptable. Letters in the figures should be 3 mm high. The figures should be presented in one of the following graphic formats: jpg, gif, pcx, bmp, tif.

REFERENCES

List of References must contain **at least 50% of articles published over the past 5 years** and **no more than 20% of links to their own work**. Cite References by number in AIP style (https://aip.scitation.org/php/authors/manuscript). Numbering in the order of referring in the text, e.g. [1], [2-5], etc. References should be listed in numerical order of citation in the text at the end of the paper (justified), Times New Roman, 9 pt, 1 spacing:

Journal Articles
[1] T. Mikolajick, C. Dehm, W. Hartner, I. Kasko, M.J. Kastner, N. Nagel, M. Moert, and C. Mazure, Microelectron. Reliab. **41**, 947 (2001), https://doi.org/10.1016/S0026-2714(01)00049-X.
[2] S. Bushkova, B.K. Ostafiychuk, and O.V. Copaiev, Physics and Chemistry of Solid State. **15**(1), 182 (2014), http://page.if.ua/uploads/pcss/vol15/!1501-27.pdf. (in Ukrainian)
[3] M. Yoshimura, E. Nakai, K. Tomioka, and T. Fukui, Appl. Phys. Lett. **103**, 243111 (2013), http://dx.doi.org/10.7567/APEX.6.052301.

E-print Resourses with Collaboration Research or Preprint
[4] M. Aaboud et al. (ATLAS Collaboration), Eur. Phys. J. C, **77**, 531 (2017), http://dx.doi.org/10.1140/epjc/s10052-017-5061-9
[5] Sjöstrand et al., *Comput. Phys. Commun.* **191,** 159 (2015), https://doi.org/10.1016/j.cpc.2015.01.024.
[6] Boudreau, C. Escobar, J. Mueller, K. Sapp, and J. Su, (2013), http://arxiv.org/abs/1304.5639.

Books
[7] S. Inoue, and K.R. Spring, *Video Microscopy*: *The fundamentals*, 2nd ed. (Plenum, New York, 1997), pp. 19-24.
[8] I. Gonsky, T.P. Maksymchuk, and M.I. Kalinsky, *Біохімія Людини [Biochemistry of Man]*, (Ukrmedknyga, Ternopil, 2002), pp. 16. (in Ukrainian)

Edited Books
[9] Z.C. Feng, editor, *Handbook of Zinc Oxide and Related Materials: Devices and Nano Engineering, vol. 2*, (CRC Press/Taylor & Francis, Boca Raton, FL, 2012)

Book Chapters
[10] P. Blaha, K. Schwarz, G.K.H. Madsen, D. Kvasnicka, and J. Luitz, in: *WIEN2K, An Augmented Plane Wave Plus Local Orbitals Program for Calculating Crystal Properties,* edited by K. Schwarz (Techn. Universität Wien, Austria, 2001).
[11] M. Gonzalez-Leal, P. Krecmer, J. Prokop, and S.R. Elliot, in: *Photo-Induced Metastability in Amorphous Semiconductors*, edited by A.V. Kolobov (Wiley-VCH, Weinheim, 2003), pp. 338-340.
[12] A. Kochelap, and S.I. Pekar, in: *Теория Спонтанной и Стимулированной Хемилюминесценции Газов [Theory of Spontaneous and Stimulated Gas Chemiluminescence]* (Naukova dumka, Kyiv, 1986), pp. 16-29. (in Russian)

Conference or Symposium Proceedings
[13] C. Yaakov, and R. Huque, in: *Second International Telecommunications Energy Symposium Proceedings*, edited by E. Yow (IEEE, New York, 1996), pp. 17-27.
[14] V. Nikolsky, A.K. Sandler, and M.S. Stetsenko, in: *Автоматика-2004: Матеріали 11 Міжнародної Конференції по Автоматичному Управлінню [Automation-2004: Materials of the 11th International Conference on Automated Management]* (NUHT, Kyiv, 2004), pp. 46-48. (in Ukrainian)

Patent
[15] I.M. Vikulin, V.I. Irha, and M.I. Panfilov, Patent Ukraine No. 26020 (27 August 2007). (in Ukrainian)

Thesis / Dissertation
[16] R.E. Teodorescu, Ph.D. dissertation, The George Washington University, 2009.

Special Notes
1. Use International System of Units (SI system). 2. It is undesirable to use acronyms in the titles. Please define the acronym on its first use in the paper. 3. Refer to isotopes as ^{14}C, ^{3}H, ^{60}Co, etc.